

# Near-bed turbulence structures in water-worked and screeded gravel-bed flows

Ellora Padhi<sup>1,a</sup>, Nadia Penna<sup>2,b</sup>, Subhasish Dey<sup>1,c</sup>, and Roberto Gaudio<sup>2,d</sup>

<sup>1</sup> *Department of Civil Engineering, Indian Institute of Technology Kharagpur, West Bengal 721302, India*

<sup>2</sup> *Dipartimento di Ingegneria Civile, Università della Calabria, 87036 Rende (CS), Italy*

Coherent structures and their impact on the near-bed time-averaged flow structure in a water-worked gravel-bed (WGB) and a screeded gravel-bed (SGB) are analyzed. Instantaneous velocities were measured using a Particle Image Velocimetry (PIV) system in the WGB and SGB flows in a flume with rectangular cross-section. To ascertain the response of the WGB with respect to the SGB to the coherent structures, the time- and double-averaged (DA) flow, and the spatially-averaged (SA) turbulence parameters, the experimental flow conditions for both the beds were kept identical. The surface gravels in the WGB were spatially organized due to the water action. By contrast, the surface gravels in the SGB were randomly poised. These result in a higher roughness height in the WGB than in the SGB. Time series analysis for the instantaneous velocity and vorticity on a central vertical plane along the streamwise direction proves that the coherent structures in the near-bed flow zone are constituted by rapidly and slowly-moving fluid streaks. Besides, the time-averaged streamwise velocity, vorticity, turbulence level, third-order correlations, and turbulent kinetic energy (TKE) budget are analyzed in the WGB and SGB. Their contours are plotted on the central vertical plane to study their spatial distributions. In addition, the SA higher-order correlations and TKE budget in the WGB and SGB are examined. Comparative study infers that the higher roughness in the WGB than in the SGB causes both the time-averaged and SA turbulence parameters in the former to be greater than those in the latter.

## I. INTRODUCTION

Geophysical flows are often found to be hydraulically rough in presence of the bed roughness elements, such as gravels, boulders etc. The existence of gravels in a stream puts significant impact on the spatial flow structures, especially in the near-bed flow zone, owing to the generation of coherent turbulence structures. Coherent structures are irregular, quasi-deterministic, and repetitive, which help to characterize the flow and govern the mean flow velocity, turbulent stress, and other statistical properties of the stream. Flow gets decelerated at the upstream of the gravels due to the action of coherent structures, while flow recirculation occurs at the downstream of the gravels.<sup>1,2</sup> It implies that the coherent structures comprise of a sequence of flow driving events,

<sup>a)</sup> [ellora@iitkgp.ac.in](mailto:ellora@iitkgp.ac.in)

<sup>b)</sup> [nadia.penna@unical.it](mailto:nadia.penna@unical.it)

<sup>c)</sup> [sdey@iitkgp.ac.in](mailto:sdey@iitkgp.ac.in)

<sup>d)</sup> Author to whom correspondence should be addressed. Electronic mail: [gaudio@unical.it](mailto:gaudio@unical.it)

40 such as ejections and sweeps.<sup>3</sup> Ejections cause the flow to decelerate by the arrival of the slowly  
41 moving fluid streaks away from the bed, while sweeps cause the flow to accelerate by the inrush  
42 of rapidly moving fluid streaks toward the streambed. Hence, the coherent structures are  
43 responsible to constitute the turbulence mechanism in a streamflow.

44 Researchers have been interested in studying the behavioral features of coherent structures due  
45 to their scientific importance.<sup>4-8</sup> Kline et al.<sup>4</sup> visualized the outbreak of near-bed low-speed  
46 coherent structures. They argued that these structures are responsible for outward transport of  
47 momentum and govern the turbulence parameters, such as Reynolds shear stress (RSS), turbulent  
48 kinetic energy (TKE) production, etc. Later, Kim et al.<sup>9</sup> extended the work of Kline et al.<sup>3</sup> to  
49 confirm that the TKE production in the near-bed flow zone occurs only during the bursting events.  
50 Inspired by these findings, researchers studied the coherent structures in hydraulically smooth  
51 flows.<sup>10-13</sup> To understand the effects of bed roughness on turbulence structures, Grass<sup>14</sup> performed  
52 experiments with turbulent flows over smooth and rough beds. They found that the characteristic  
53 feature of the coherent structures is influenced by the bed roughness. Further, Drake et al.<sup>15</sup>  
54 captured the bedload transport process using a high-speed camera and visualized the sediment  
55 motion that was affected by the downward motion of rapidly moving fluid streaks (sweeps). Grass  
56 et al.<sup>16</sup> showed the presence of coherent structures in the rough-turbulent boundary-layer flow and  
57 linked them with the bursting events. Later, Nezu and Nakagawa<sup>17</sup> studied the coherent structures  
58 to distinguish the near-bed flow fields corresponding to small-scale turbulent events from the far-  
59 bed large-scale vortical structures. In recent decades, several researchers tried to analyze, both  
60 experimentally and numerically, the characteristics of the coherent structures for different open-  
61 channel flow conditions, such as permeable bed flow,<sup>18-20</sup> flow within vegetation canopy,<sup>21-24</sup>  
62 flow past a bluff body,<sup>25-27</sup> mobile bed flow,<sup>28-30</sup> and gravel-bed flow.<sup>1,31-35</sup>

63 Moreover, in case of gravel-bed flow, although significant progress has so far been made to  
64 study the effects of coherent structures on turbulence parameters, only a few important turbulence  
65 parameters were taken into consideration. To be specific, Buffin-Bélanger et al.<sup>36</sup> performed space-  
66 time correlation analysis considering the velocity fluctuations to show the presence of large-scale  
67 flow structures in gravel-bed flows. Roy et al.<sup>1</sup> conducted field experiments to quantify the vertical,  
68 spanwise and streamwise extents of the flow structures and to estimate their advecting velocities.  
69 Hurther et al.<sup>31</sup> showed the presence of large-scale coherent structures in gravel-bed flows  
70 examining the instantaneous velocity. In addition, they studied the effects of coherent structures  
71 on the TKE production and fluxes. Detert et al.<sup>33</sup> observed the coherent structures in gravel-bed  
72 flows in the form of wedge like structures, which are composed of slowly and rapidly moving fluid  
73 streaks. However, they did not analyze the effects of coherent structures on turbulence parameters.  
74 Further, Guala et al.<sup>34</sup> confirmed the existence of vortex packets in the outer-layer of a rough-flow  
75 by performing an experimental study on sparse roughness elements, which cause a shortening of  
76 the streamwise length scale in the near-bed flow. Recently, Voermas et al.<sup>35</sup> used conditional  
77 sampling method to separate the motions of coherent structures based on the bursting events.  
78 However, the study was limited to the instantaneous flow velocity and the RSS. Hence, the impact  
79 of these conditionally sampled coherent structures on the time- and double-averaged (DA) flow  
80 parameters were not considered. Moreover, in a gravel-bed flow, the near-bed flow is locally three-  
81 dimensional and heterogeneous in space due to the fluid-gravel interaction, making the analysis of  
82 near-bed turbulence parameters complicated. Having understood the complexity, researchers  
83 investigated the gravel-bed flow and analyzed the turbulence parameters in terms of DA velocity,  
84 spatially-averaged (SA) RSS, SA Reynolds normal stresses, TKE fluxes, TKE budget, etc.<sup>37-43</sup>

84 Although aforementioned studies provide an insight into the near-bed flow field in gravel-bed  
85 flows, the visualization of coherent structures, spatial variations of the time-averaged flow  
86 parameters, turbulence level, and higher-order correlations in gravel-bed flows are still to be  
87 explored in detail. To date, most of the experimental studies on gravel-bed flows have been  
88 conducted by dispersing the gravel mixtures in the flumes and then screeding them manually. The  
89 bed topographies of such *screeded gravel-beds* (SGBs) are dissimilar from those observed in  
90 natural gravel-bed streams. In a natural stream, continuous erosion and deposition of gravel occur  
91 due to repetitive floods. As a result, a gravel-bed roughness structure is created by the flowing  
92 water, and such a bed is termed *water-worked gravel-bed* (WGB). The bed surface in a WGB  
93 possesses a spatially multifaceted, three-dimensional, well-organized roughness structure. Hence,  
94 such a WGB surface roughness is entirely different from that created manually (SGB) in a  
95 laboratory flume.<sup>44,45</sup> Importantly, three-dimensional information is required to accurately  
96 characterize the bed roughness structures.<sup>46</sup> Recently, Padhi et al.<sup>45,47</sup> reported that the surface  
97 topography is one of the significant parameters that influence the near-bed profiles of SA  
98 turbulence parameters. It is pertinent to mention that during the special averaging of a quantity, its  
99 flow features in the spatial domain remain missing. Hence, to visualize the motions of coherent  
100 structures and to precisely understand their impact on the near-bed spatial flow structure, it is  
101 essential to examine the spatial flow structure including the turbulence parameters over a WGB.

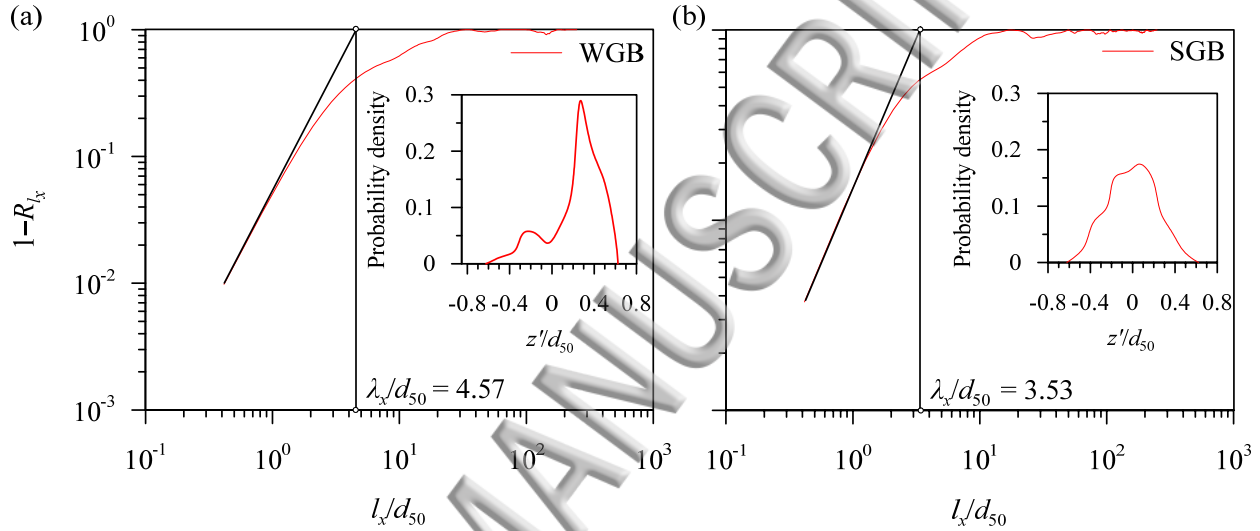
102 Therefore, the aim of this study is to capture the motions of the coherent structures by  
103 performing the time series analysis and to analyze their impact on the near-bed time-averaged flow  
104 field. In doing so, an experimental study was carried out in a WGB capturing the flow field by a  
105 Particle Image Velocimetry (PIV) system. Further, to understand the effects of the difference in  
106 bed roughness height on the coherent structures, an additional experimental study was carried out  
107 in an SGB, keeping the flow condition alike the WGB. Using the experimental data, the contours  
108 of instantaneous and time-averaged vorticities, turbulence level, DA degree of anisotropy, SA  
109 second- and third-order correlations, and TKE budget in both the beds are analyzed and compared.  
110 Thus, this study provides an insight into the near-bed flow physics governed by the coherent  
111 structures and the impact of bed roughness on the SA turbulence parameters in the WGB and SGB.

## 112 113 **II. EXPERIMENTAL SETUP AND PROCEDURE**

114  
115 Experiments were carried out in a recirculating tilting flume with a rectangular cross-section of  
116 length 9.6 m, width 4.85 m and height 0.5 m located at the *Grandi Modelli Idraulici* laboratory,  
117 Università della Calabria, Italy. The flume entrance comprised of a stilling tank, an uphill spillway,  
118 and honeycombs (10 mm diameter) to minimize the instabilities in flow at the entry. The size of  
119 the honeycomb was chosen in a manner that satisfied the general criteria for turbulent flow  
120 measurements.<sup>48,49</sup> A hydraulic jack was operated to fix the bottom slope of the flume. The flow  
121 velocity was controlled by adjusting the pumping rate of flow. In order to maintain the flow depth  
122  $h$ , an adjustable tailgate was operated at the flume outlet. Downstream of the tailgate, a sediment  
123 trap was placed to collect the transported gravel particles. A triangular weir was used to meter the  
124 flow discharge. The flume side-walls were made of transparent glass to visualize the flow. The test  
125 section, located at 7.18 m downstream of the flume entrance, was 0.12 m long. Here the flow was  
126 observed to be fully-developed. The detailed experimental setup was reported in Padhi et al.<sup>45</sup>

127 For the preparation of the experimental bed, coarse gravel with a median size  $d_{50}$  of 4.81 mm  
128 was used as bed material. At the beginning of the experiment, gravel was dispersed on the flume  
129 bottom and screeded manually to create an SGB. The bed topography in the SGB was measured

131 using a Leica ScanStation P20 laser scanner with an accuracy of less than  $\pm 3$  mm. From the bed  
 132 surface fluctuation data, the average bed slope in the SGB was determined to be 0.7%.  
 133 Subsequently, the WGB was created by the flow over an SGB that could move the surface gravels.  
 134 Having achieved the final equilibrium condition, the bed topography was again measured by the  
 135 laser scanner. The average bed slope in the WGB was obtained to be 0.4%. The detailed description  
 136 of the preparation of the WGB was described in Padhi et al.<sup>45</sup> Analyzing the bed surface fluctuation  
 137 data in the WGB and SGB, the average roughness heights  $\Delta_k$  of both the beds were obtained from  
 138 the standard deviation of bed surface fluctuations. In the WGB and SGB, the values of  $\Delta_k$  were  
 139 1.25 mm and 1.04 mm, respectively.



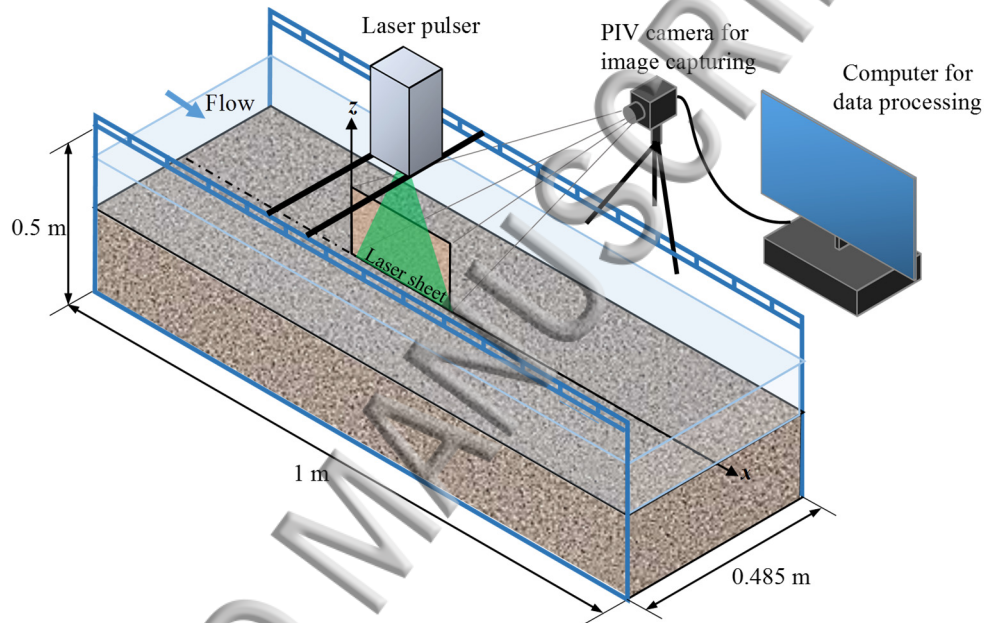
140  
 141  
 142 FIG. 1. Dependencies of residual autocorrelation function ( $1 - R_{l_x}$ ) on dimensionless streamwise  
 143 spacing  $l_x/d_{50}$  in the (a) WGB and (b) SGB. The probability density functions of bed surface  
 144 fluctuations as a function of dimensionless bed surface fluctuation  $z'/d_{50}$  are presented in the insets  
 145 in the (a) WGB and (b) SGB.

146  
 147 Further, to characterize the bed roughness structures,<sup>50</sup> the autocorrelation function  $R_{l_x}$  can be  
 148 computed to define the horizontal length scales  $\lambda_x$  of bed surface fluctuations in both the beds as

149  
 150 
$$R_{l_x} = \frac{1}{N - n} \sum_{i=1}^{N-n} [z'(x_i)z'(x_i + n\delta x)], \quad (1)$$

151  
 152 where  $l_x$  is the sampling length in streamwise direction ( $= n\delta x$ ),  $x$  is the streamwise distance from  
 153 a convenient location,  $i = 1, 2, 3, \dots, n$ ,  $n$  is the number of points in streamwise direction,  $N$  is the  
 154 total number of points in streamwise direction, and  $\delta x$  is the sampling interval considered as 2 mm,  
 155 and  $z'$  is the bed surface fluctuation with respect to mean surface elevation. Dependencies of the  
 156 residual autocorrelation function ( $1 - R_{l_x}$ ) on dimensionless streamwise spacing  $l_x/d_{50}$  in the WGB  
 157 and SGB are shown in Figs. 1(a) and 1(b), respectively. The horizontal length scales  $\lambda_x$  are  
 158 obtained as  $\lambda_x = 4.57d_{50} = 0.022$  m in the WGB and  $\lambda_x = 3.53d_{50} = 0.017$  m in the SGB. It suggests  
 159 that the roughness elements (surface gravels) in the WGB had an affinity to orient their longest

161 along the streamwise direction, while in the SGB, they were observed to be randomly poised  
162 without any directional preferences. Additionally, the probability density functions of  
163 dimensionless bed surface fluctuation  $z'/d_{50}$  along the flume centerline in the WGB and SGB are  
164 provided in the inset of Figs. 1(a) and 1(b), respectively. It is apparent that the roughness structures  
165 in both the WGB and SGB follow the asymmetric distributions. To be specific, the WGB bed  
166 roughness structure is negatively skewed, while the SGB bed roughness structure is positively  
167 skewed. It implies that due to the water action, the bed topography in the WGB was fairly different  
168 from that in the SGB. Moreover, to ascertain the effects of difference in bed roughness on the  
169 turbulent flow field, two experimental runs were taken over the WGB and SGB, keeping the flow  
170 conditions identical.



171  
172  
173 FIG. 2. Schematic of the flume test section showing the flow measuring devices.  
174

175 Figure 2 shows the schematic of the test section with the flow measuring devices. To measure  
176 the flow field, a two-dimensional PIV system manufactured by Trust Science Innovation - TSI  
177 Incorporated was used. It consisted of a Nikon 12 bit CCD camera (50 mm F1.8 lens, aperture  
178 opening of  $f/16$ ,  $2048 \times 2048$  pixel<sup>2</sup> resolution and frame rate of 15 Hz) and a double pulse  
179 Nd:YAG laser, having a pulse energy of 200 mJ at a wavelength of 532 nm. Because of the PC  
180 port frequency limitation, the PIV system was operated at 7.5 Hz. Titanium dioxide (TiO<sub>2</sub>), having  
181 a mean size of 3  $\mu\text{m}$  and a relative density of 4.26, was used to seed the flow. The test section was  
182 illuminated with the laser to capture the motion of the seeding particles by the Nikon camera placed  
183 parallel to the laser sheet with a lens-centerline (cross-hair) elevation of 5 cm from the average bed  
184 level, enabling us to identify the flow below the crest. It can be noted that close to the flume-wall,  
185 the camera visual field for few points was blocked by the adjacent gravels. Therefore, it was  
186 impossible to acquire the velocity data where the view was blocked. The flow measurements were  
187 taken over a span of 120 mm on a central vertical plane of the flume along the streamwise direction,  
188 capturing 3000 pairs of images over a period of 414 s. The overall area of the captured image was

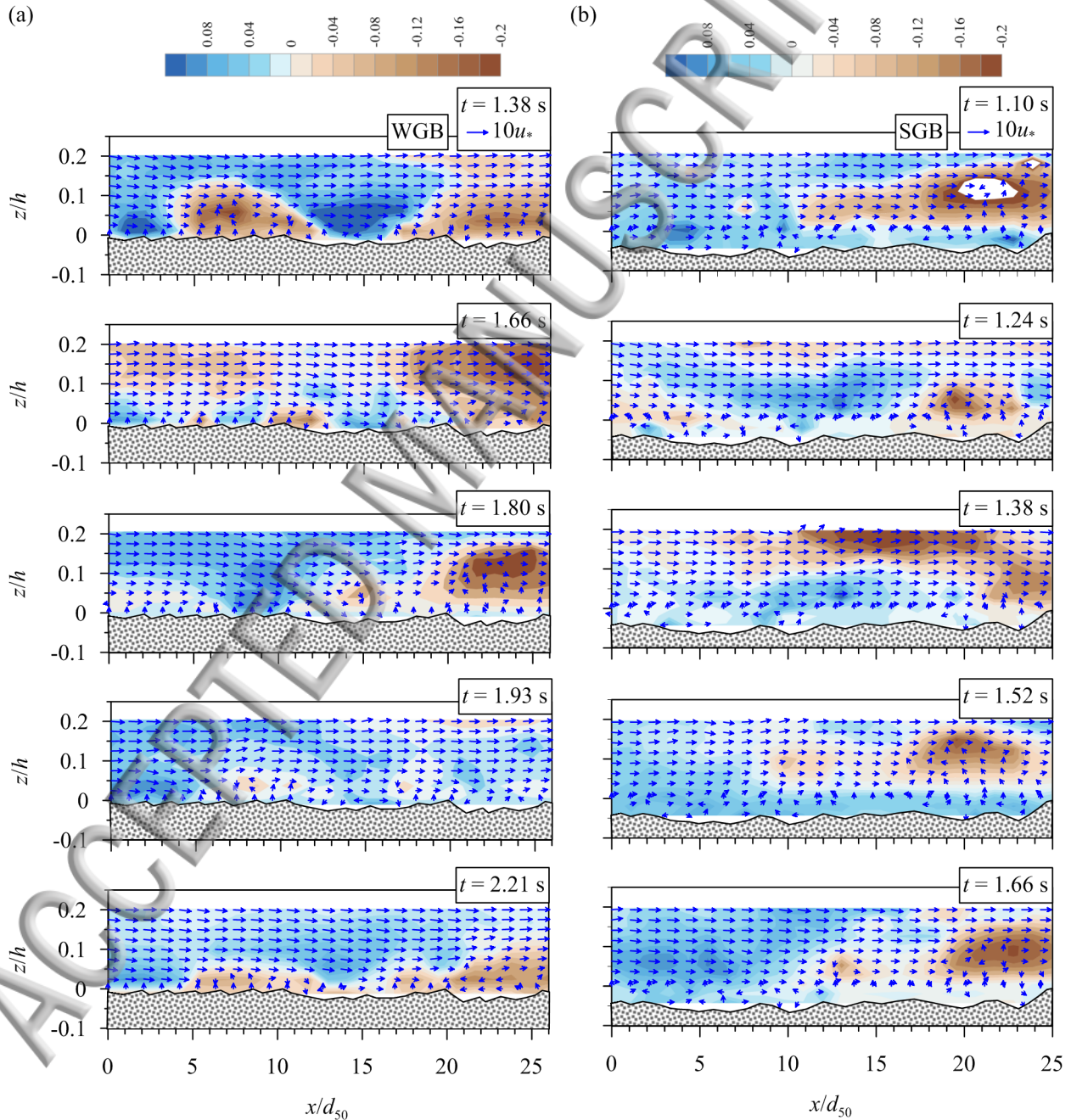
185  $120 \times 170 \text{ mm}^2$  with an interrogation area of  $64 \times 64 \text{ pixel}^2$ . The image analysis provided  
190 approximately forty-three velocity profiles on a vertical plane, covering an area of  $120 \times 100 \text{ mm}^2$   
191 with a spatial resolution of 2.7 mm in both the horizontal and vertical directions.

192 Flow measurements in the WGB and SGB were carried out with a flow depth  $h$  of 0.1 m  
193 (measured from the gravel crest) and an average flow velocity  $U_{avg}$  [=  $Q/(Bh)$ , where  $Q$  is the flow  
194 discharge and  $B$  is the flume width] of  $0.43 \text{ m s}^{-1}$ . The  $U_{avg}$  was less than the critical flow velocity  
195  $U_c$  ( $= 0.6 \text{ m s}^{-1}$ ) for the initiation of gravel motion, computed from Neill's formula,<sup>51</sup> which is  $U_c$   
196  $= 1.41(\Delta g d_{50})^{0.5}(h/d_{50})^{1/6}$ ; where  $\Delta$  is the submerged relative density of gravel. Thus, a clear-water  
197 condition prevailed during the flow measurements. The shear velocity  $u^*$  [=  $(-\langle u'w' \rangle)^{0.5}$ , where  $u'$   
198 and  $w'$  are the fluctuations of streamwise and vertical velocity components with respect to their  
199 time-averaged values, respectively] in the WGB and SGB were obtained from the RSS profiles to  
200 be  $0.068 \text{ m s}^{-1}$  and  $0.077 \text{ m s}^{-1}$ , respectively, as reported in Padhi et al.<sup>45</sup> Note that the time-  
201 averaged quantity means the time independent averaged value of the quantity obtained by  
202 averaging over a sufficiently long period of time. The flow Froude number  $Fr$  [=  $U_{avg}/(gh)^{0.5}$ ,  
203 where  $g$  is the gravitational acceleration] and the flow Reynolds number  $R$  ( $= 4U_{avg}h/\nu$ , where  $\nu$  is  
204 the water kinematic viscosity, taken as  $10^{-6} \text{ m}^2 \text{ s}^{-1}$ ) were determined to be 0.432 and  $1.75 \times 10^5$ ,  
205 respectively. In addition, the shear Reynolds numbers  $R^*$  ( $= u^* \Delta k/\nu$ ) in the WGB and SGB were  
206 calculated as 85 and 81, respectively, being greater than 70, confirming the rough-turbulent flow  
207 to be prevalent. To ascertain the two-dimensionality of the flow field in the central part of the  
208 flume, flow measurements were conducted at four different spanwise locations along the  
209 streamwise direction of the test section. The DA streamwise velocity and SA RSS profiles reveal  
210 that at least in the central portion of the flume ( $\pm 0.075 \text{ m}$  off the centerline), the two-dimensionality  
211 of the flow was satisfactorily preserved in both the beds.

### 212 213 III. INSTANTANEOUS AND TIME-AVERAGED VELOCITY FIELDS 214

215 In the wall-shear layer, the turbulent eddies forming the *coherent structures* prevail.<sup>52,53,54</sup> They  
216 appear as recursive spatially-temporal flow structures to contribute to the time-averaged flow.  
217 They are the primary cause of the TKE production in a turbulent flow.<sup>16</sup> Such structures are self-  
218 perpetual and thus deemed to be cyclic phenomena. To this end, the sequence of five consecutive  
219 instantaneous flow fields at different times  $t$  forming a cyclic process in the WGB and SGB are  
220 displayed in Figs. 3(a) and 3(b), respectively. Dimensionless instantaneous velocity vectors,  
221 having magnitude  $(u^2 + w^2)^{0.5}/u^*$  and direction  $\tan^{-1}(w/u)$ , represent the instantaneous flow fields  
222 in the WGB and SGB. Here,  $u$  and  $w$  are the instantaneous streamwise and vertical velocity  
223 components, respectively. The abscissa refers to the streamwise distance  $x$  and the ordinate to the  
224 vertical distance  $z$  from the crest level are scaled by  $d_{50}$  and  $h$ , respectively. In Figs. 3(a) and 3(b)  
225 (and the subsequent figures related to the spatial flow structures), the spatial flow domains are  
226 exhibited for the wall-shear layer portion ( $z \leq 0.2h$ ) in order to focus on the roughness influenced  
227 flow structures. In both the WGB and SGB, the near-bed flow heterogeneity is evident from the  
228 frequent changes of magnitude and direction of velocity vectors. They indicate that both the  
229 upward and downward temporal motions prevail over the entire reach. The downward velocity  
230 vectors suggest an arrival of rapidly moving fluid streaks, while the upward velocity vectors  
231 signify the arrival of slowly moving fluid streaks. Besides, the velocity vectors are scattered due  
232 to the local bed undulations, indicating the formation of recirculation zones, where the flow retards.  
233 In addition, in order to precisely assess the instantaneous flow field with respect to time-averaged

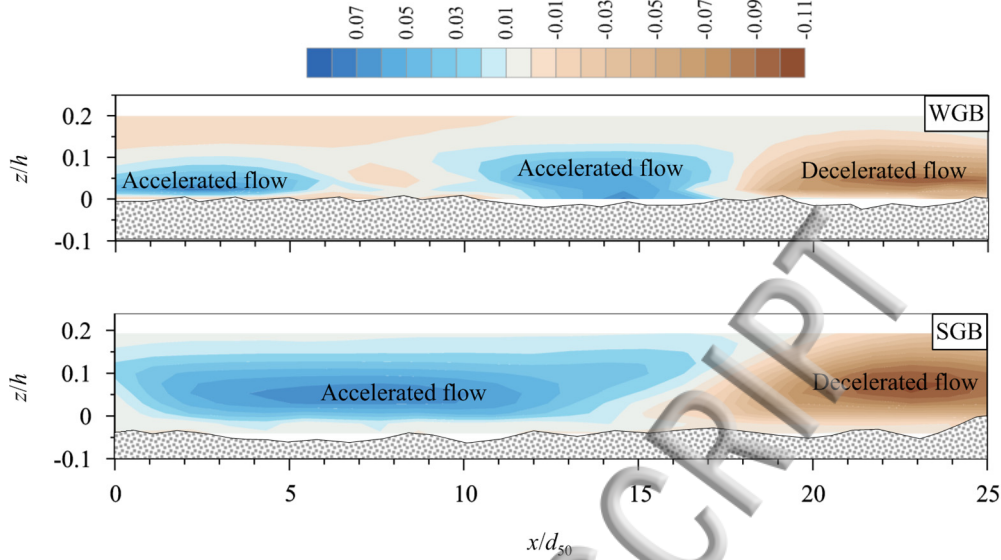
235 However, the spatial flow domain is divided into the accelerated and decelerated flow zones. The  
 236 accelerated flow zone refers to the zone, where the instantaneous flow velocity  $(u^2 + w^2)^{0.5}$  at a  
 237 given time  $t$  exceeds the time-averaged flow velocity  $\bar{U} [= (\bar{u}^2 + \bar{w}^2)^{0.5}]$ , where  $\bar{u}$  and  $\bar{w}$  are the  
 238 time-averaged streamwise and vertical velocity components, respectively] in an instantaneous flow  
 239 field. Likewise, the decelerated flow zone is the zone, where  $(u^2 + w^2)^{0.5}$  is less than  $\bar{U}$ . Hence,  
 240 considering these criteria, the contours of accelerated and decelerated flow are plotted in the WGB  
 241 and SGB [Figs. 3(a) and 3(b)]. It may be noted that the accelerated flow zone is referred to as  
 242 sweeps dominance zone, while the decelerated flow zone is referred to as ejections ascendency  
 243 zone.<sup>33</sup>



244

246 FIG. 3. Dimensionless instantaneous velocity vectors, having magnitude  $(u^2 + w^2)^{0.5}/u_*$  and  
247 direction  $\tan^{-1}(w/u)$ , at different times  $t$  on a vertical central plane in the (a) WGB and (b) SGB.  
248 The color bars represent the values of  $[(u^2 + w^2)^{0.5} - \bar{U}] u_*^{-1}$ , where the contours of accelerated  $[(u^2$   
249  $+ w^2)^{0.5} - \bar{U}] u_*^{-1} > 0$  and decelerated  $[(u^2 + w^2)^{0.5} - \bar{U}] u_*^{-1} < 0$  flows are shown in blue and brown  
250 colors, respectively.  
251

252 In the WGB [Fig. 3(a)], at  $t = 1.38$  s (starting time of a cycle), the accelerated flow rolls over  
253 the decelerated flow zone owing to a higher velocity at a length scale of approximately  $10d_{50}$  ( $\approx$   
254  $2\lambda_x$ ). The accelerated flow dominates the flow field until it encounters a recirculation zone, where  
255 the flow starts decelerating. Hence, the decelerated flow in the subsequent flow field at  $t = 1.66$  s  
256 becomes the dominant flow in the entire flow reach. The time scale to changeover to this flow  
257 regime is  $\Delta t = 0.28$  s. However, the dominance of the decelerated flow is not persistent, as apparent  
258 from the following flow field at  $t = 1.80$  s, because the rapidly moving fluid streaks inrush toward  
259 the bed, diminishing the decelerating flow effects. This change occurs at a shorter time scale of  $\Delta t$   
260  $= 0.14$  s. Gradually, it gives rise to the accelerated flow zone, which spreads and almost occupies  
261 the entire flow reach. To be explicit, the entire flow reach at  $t = 1.93$  s is returned to be dominated  
262 by the accelerated flow, nullifying the decelerating effects. This changeover takes place at almost  
263 similar time scale ( $\Delta t = 0.13$  s) of the previous sequence. On the other hand, the decelerated flow  
264 recurs by entraining the slowly moving fluid streaks into the upper flow zone, as evident from the  
265 flow field at  $t = 2.21$  s (ending time of the cycle). Importantly, the time scale to changeover to this  
266 flow regime is the same as that in the first sequence, that is  $\Delta t = 0.28$  s. Interestingly, it is noticeable  
267 that the first (at  $t = 1.38$  s) and last (at  $t = 2.21$  s) flow fields look quite similar, indicating the  
268 recurrence of the cyclic coherent structures at a certain time interval (0.83 s). However, during the  
269 changeover in the intermediate sequences ( $t = 1.66, 1.80$  and  $1.93$ ), the flow features do not follow  
270 any specific length scale. Similar observations can also be made from the vector and contour plots  
271 in the SGB for the sequence of times  $t = 1.10$  to  $1.66$  s, but at a shorter recurring time interval  
272 (0.56 s) than that in the WGB [Fig. 3(b)]. In the SGB, the time scales to changeover for all the  
273 sequences are the same ( $\Delta t = 0.14$  s). Comparing the velocity vectors in both the beds, it is evident  
274 that the near-bed velocity vectors in the WGB are less scattered than those in the SGB. The reason  
275 is attributed to roughness structure in the WGB being well organized, aligning their longest axis  
276 streamwise, as reflected from the longer horizontal length scales  $\lambda_x$  in the WGB than in the SGB.  
277 On the other hand, the SGB roughness structure is randomly poised and does not have any  
278 directional preferences. This causes to have a more perturbed near-bed flow structure in the SGB  
279 that has an indistinguishable length scale. In essence, the coherent structures in both the WGB and  
280 SGB are the irregular, but repetitive structures, recurring at a certain time interval, which is longer  
281 in the WGB than in the SGB.  
282



283  
284

285 FIG. 4. Contours of dimensionless time-averaged accelerated  $(\bar{U} - \langle \bar{U} \rangle) u_*^{-1} > 0$  and decelerated  $(\bar{U} - \langle \bar{U} \rangle) u_*^{-1} < 0$  flows on a vertical central plane in the WGB and SGB.

287

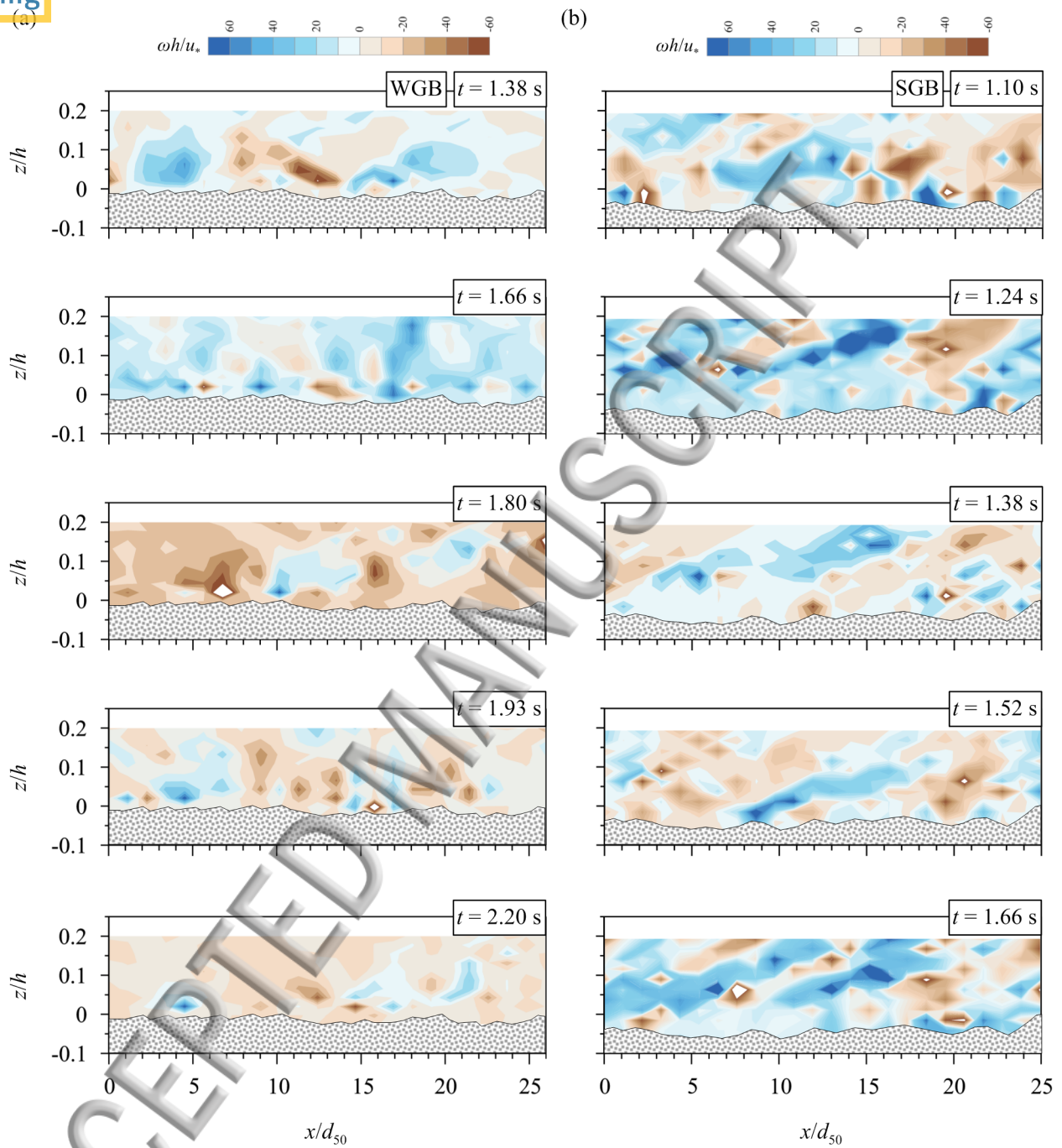
288 To analyze the time-averaged flow velocity field with respect to the DA flow velocity in a  
289 spatial flow domain, Fig. 4 shows the contours of dimensionless time-averaged accelerated and  
290 decelerated flows on a vertical central plane in the WGB and SGB. In this study, the time-averaged  
291 flow is considered to be accelerated if  $(\bar{U} - \langle \bar{U} \rangle) u_*^{-1} > 0$  and decelerated if  $(\bar{U} - \langle \bar{U} \rangle) u_*^{-1} < 0$ , where  
292  $\langle \bar{U} \rangle = (\langle \bar{u} \rangle^2 + \langle \bar{w} \rangle^2)^{0.5}$ , and  $\langle \bar{u} \rangle$  and  $\langle \bar{w} \rangle$  are the DA streamwise and vertical velocities, respectively.  
293 In the DA methodology, an area averaging of the time-averaged velocities is performed over the  
294 layer parallel to the mean bed surface, as was done by Padhi et al.<sup>45</sup> It is apparent in Fig. 4 that in  
295 both the beds, there exist alternate zones of time-averaged accelerated and decelerated flows,  
296 having a longer zonal distributions in the SGB [at a length scale of approximately  $15d_{50}$  ( $\approx 3\lambda_x$ )]  
297 than in the WGB [at a length scale of approximately  $10d_{50}$  ( $\approx 2\lambda_x$ )]. A close examination of the  
298 contours reveal the decelerated flow zones, regarded as recirculation zones, appear downstream of  
299 the accelerated flow zones at  $x = 18d_{50}$  in the WGB and  $x = 15d_{50}$  in the SGB. It can be concluded  
300 that the time-averaged flow features in the WGB have a shorter length scale than in the SGB.

301

#### 302 IV. INSTANTANEOUS AND TIME-AVERAGED VORTICITIES

303

304 The contours of dimensionless instantaneous vorticity  $\omega h/u_*$  on a vertical central plane at  
305 different times  $t$  in the WGB and SGB are presented in Figs. 5(a) and 5(b), respectively. Here,  $\omega$   
306 represents the instantaneous vorticity, given by  $\partial u/\partial z - \partial w/\partial x$ , whose positive and negative values  
307 specify the clockwise and counterclockwise fluid motions, respectively.<sup>2</sup> Further, the  
308 counterclockwise fluid motion causes the flow to accelerate, resulting in a downward transport of  
309 momentum in the downstream direction. On the other hand, the clockwise fluid motion causes the  
310 flow to decelerate, resulting in an upward transport of momentum in the upstream direction. These  
311 motions of the fluid momentum (streaks) are responsible for the RSS production.<sup>55, 56</sup>



313  
314  
315  
316  
317  
318  
319

FIG. 5. Contours of dimensionless instantaneous vorticity  $\omega h/u_*$  at different times  $t$  on a vertical central plane in the (a) WGB and (b) SGB. The contours of clockwise (positive  $\omega$ ) and counterclockwise (negative  $\omega$ ) instantaneous vorticity are shown in blue and brown colors, respectively.

Reverting to Fig. 5(a) for the WGB case, at  $t = 1.38$  s, the vorticity  $\omega$  changes its sign from positive to negative in an alternative manner, at a length scale of approximately  $10d_{50}$  ( $\approx 2\lambda_x$ ), by balancing each other along the entire reach. A recirculation zone is created (as discussed earlier), due to the variable local bed undulations. It induces the fluid streaks to rotate in a clockwise direction, causing the flow to decelerate. This indicates to initiate the ejections. In the subsequent instant at  $t = 1.66$  s, the retarding effects due to flow recirculation persist that can be inferred from the rotational sense of vortical structures and the ejections prevail. However, this scenario does not last long, because the rapidly moving fluid streaks inrush toward the bed. This can be inferred from the vorticity contours at  $t = 1.8$  s. As a result, the clockwise vortices change their rotational sense to counterclockwise. This causes the flow to accelerate, inducing the sweeps. Then, at  $t = 1.93$  s, the rapidly moving fluid streaks again encounter the recirculating flow zone, which annihilates the effects of sweeps and induces the slowly moving fluid streaks. In the next instant at  $t = 2.20$  s, there exist both clockwise and counterclockwise motions of the fluid streaks in an alternative manner, as it was observed in the first vorticity contours at  $t = 1.38$  s. It implies that the vortical structures are recursive in nature, regenerating at a certain time interval. In the SGB [Fig. 5(b)], the depictions of the vorticity contours are almost similar to those in the WGB for the sequence of times  $t = 1.10$  to  $1.66$  s, but at a shorter recurring time interval than that in the WGB. Nevertheless, in the SGB, unlike the WGB, clockwise and counterclockwise motions of fluid streaks are not distinctively alternative in the vorticity contours at different time. The reason is ascribed to the randomly poised roughness elements (gravels) in the SGB.

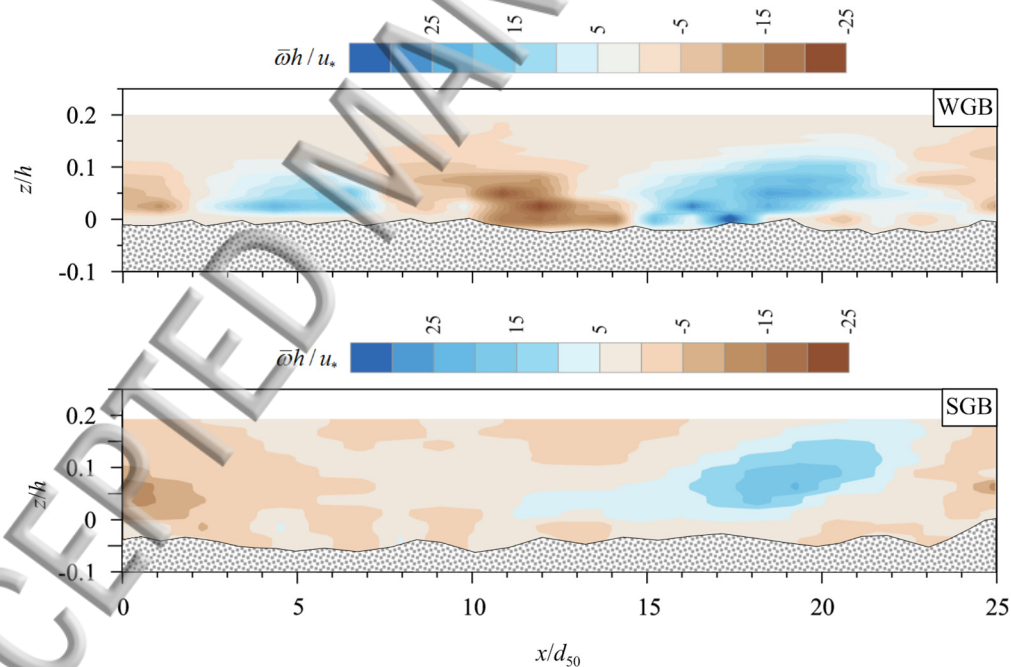


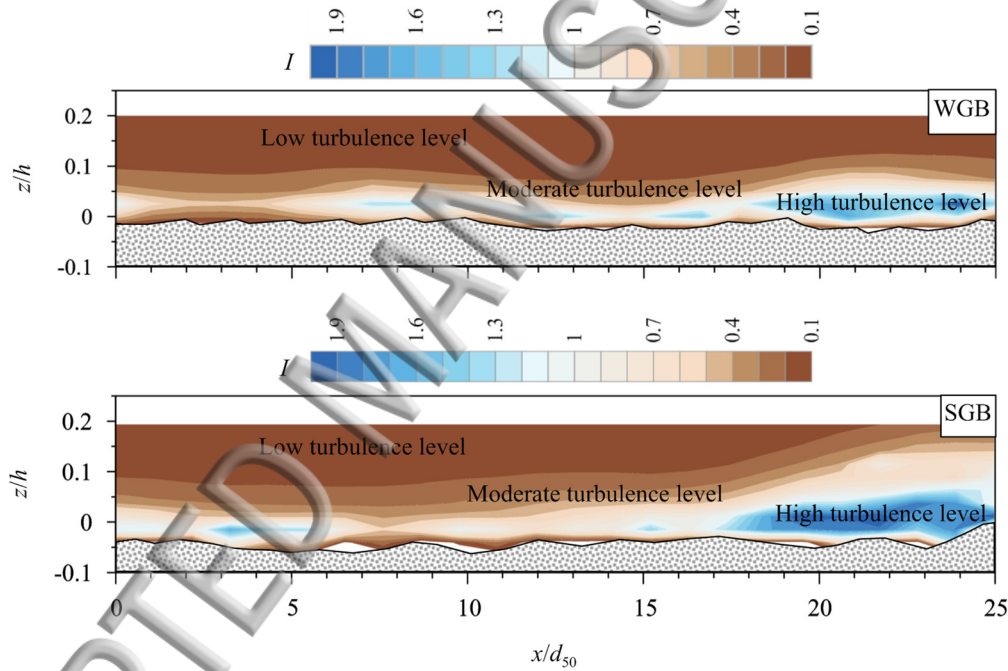
FIG. 6. Contours of dimensionless time-averaged vorticity  $\bar{\omega} h / u_*$  on a vertical central plane in the WGB and SGB.

To substantiate the effects of bed roughness structures, Fig. 6 depicts the contours of dimensionless time-averaged vorticity  $\bar{\omega} h / u_*$  on a vertical central plane in the WGB and SGB.

348 re,  $\bar{\omega}$  is the time-averaged vorticity, given by  $\partial\bar{u}/\partial z - \partial\bar{w}/\partial x$ . It is apparent that the  $\bar{\omega}$  changes  
 349 its sign alternatively along the entire stretch of the measuring section. It implies that the gravels  
 350 cause the time-averaged near-bed flow to be heterogeneous, activating the fluid streaks to have  
 351 motions alternatively in both clockwise and counterclockwise directions. The changes of the  
 352 rotational sense of time-averaged vortices are spatially more frequent [at a length scale of  
 353 approximately  $10d_{50}$  ( $\approx 2\lambda_x$ )] in the WGB than in the SGB.

### 355 V. TIME-AVERAGED AND SPATIALLY-AVERAGED TURBULENCE INDICATORS

356  
 357 The time-averaged turbulence indicator  $I$  is one of the most useful tools to measure the local  
 358 turbulence level in a turbulent flow. It can be estimated as  $I = [(2/3)k]^{0.5}/\bar{U}$ , where  $k$  is the TKE.  
 359 For a two-dimensional PIV data, the  $k$  can be approximated as  $0.75(u'u' + w'w')$ ,<sup>47,57,58</sup> because  
 360 the measurement of spanwise velocity  $v$  was unavailable. The turbulence level is deemed to be  
 361 high if  $I = 0.5-2$ , moderate if  $I = 0.1-0.5$  and low if  $I < 0.1$ .<sup>59,60</sup>

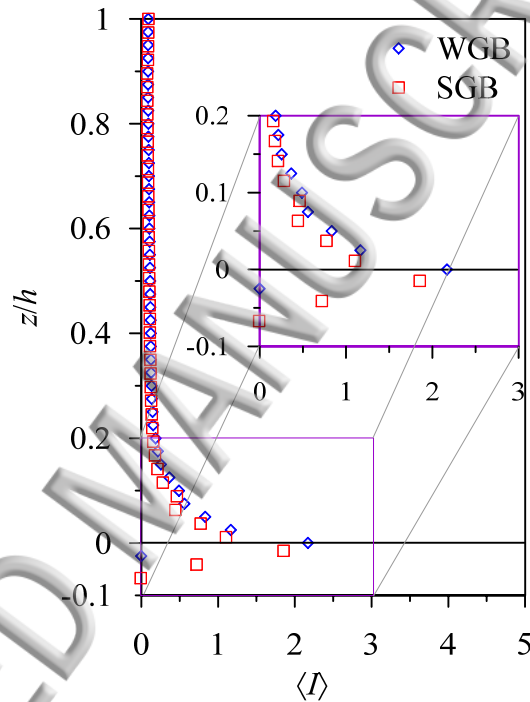


363  
 364  
 365 FIG. 7. Contours of time-averaged turbulence indicator  $I$  on a vertical central plane in the WGB  
 366 and SGB.

367  
 368 The contours of time-averaged turbulence indicator  $I$  on a vertical central plane in the WGB  
 369 and SGB are displayed in Fig. 7. In both the beds, the magnitudes of  $I$  are very high in the near-  
 370 bed flow zone, where bed roughness provokes the turbulence. However, it decreases gradually, as  
 371 one moves toward the top edge of the wall-shear layer ( $z = 0.2h$ ). In the WGB, the high turbulence  
 372 level starts from the flow zone below the crest level and is extended up to  $z = 0.05h$ . Thereafter, a  
 373 moderate turbulence level starts and continues up to the top edge of the form-induced sublayer ( $z$   
 374  $= 0.1h$ , as reported in Padhi et al.<sup>45</sup>). It implies that the  $u'$  and  $w'$  get excited by the gravels, causing  
 375 an enhanced turbulence level in the vicinity of the crest. Conversely, for  $z > 0.1h$ , the turbulence

level becomes low. Nevertheless, as the vertical distance increases, the roughness effects induced by gravels on the flow diminish due to the damping in  $u'$  and  $w'$ . Akin to the WGB, in the near-bed SGB flow zone ( $-0.06h < z < 0.05h$ ), the turbulence level is high. Above that, a moderate turbulence level zone appears. However, unlike the WGB, the moderate turbulence level zone in the SGB is somewhat spatially nonuniform. As a result, it extends up to the top edge of the wall-shear layer at the end of the measuring section. On the other hand, the low turbulence level zone starts from  $z = 0.05h$ . It gradually decreases as one moves in the streamwise direction. The possible reason is accredited to the randomly composed surface gravels in the SGB. Further, the comparison between two contour plots infers that although the WGB possesses higher roughness than the SGB, the distributions of the turbulence levels in the WGB are apparently more spatially homogeneous over the streamwise distance than those in the SGB.

387



388

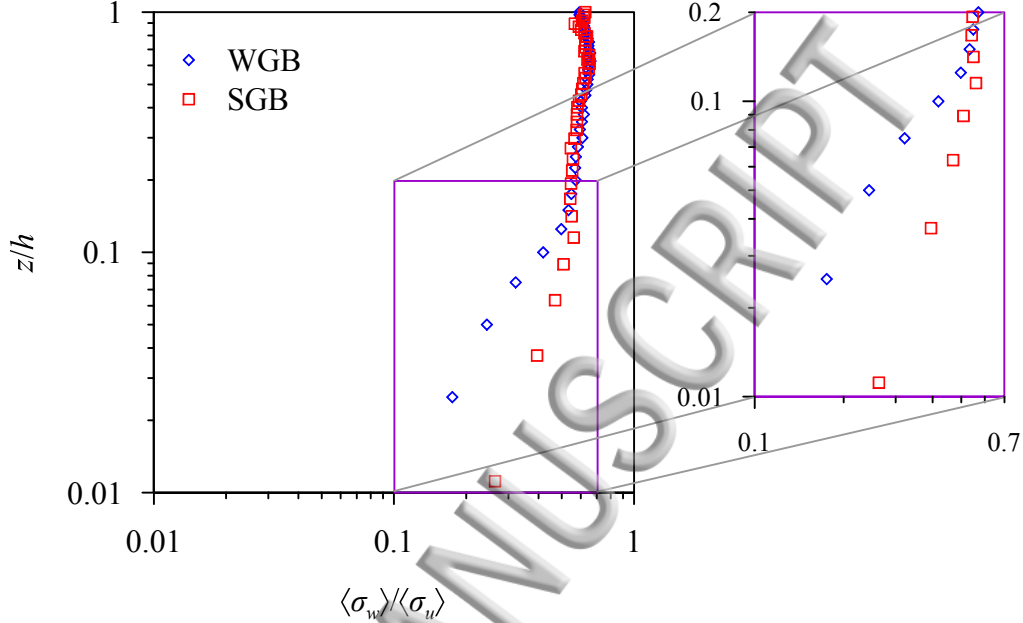
389

390 FIG. 8. Variations of SA turbulence indicator  $\langle I \rangle$  with dimensionless vertical distance  $z/h$  in the  
391 WGB and SGB.

392

393 In a heterogeneous turbulent flow, the SA turbulence indicator  $\langle I \rangle$  is expressed as  
394  $[(2/3)\langle k \rangle]^{0.5}/\langle \bar{U} \rangle$ , where  $\langle k \rangle$  and  $\langle \bar{U} \rangle$  are the SA TKE and DA flow velocity, respectively. It provides  
395 information on the overall turbulence level within the flow domain across the flow depth. Figure  
396 8 depicts the variations of SA turbulence indicator  $\langle I \rangle$  with  $z/h$  ( $= -0.1$  to  $1$ ) in the WGB and SGB.  
397 In the inset, the variations are shown up to  $z/h = 0.2$  in order to have their enlarged views within  
398 the wall-shear layer. In both the beds, the  $\langle I \rangle$  profiles that start developing beneath the crest level  
399 increase sharply with an increase in  $z$ , attaining their peaks near the crest. To be specific, the  $\langle I \rangle$   
400 profile in the WGB attains its peak at the crest, while in the SGB, the peak appears just below the  
401 crest. Then, the  $\langle I \rangle$  profiles decrease with a further increase in  $z$ , becoming almost independent of  
402  $z$  for  $z > 0.2h$ . The  $\langle I \rangle$  values in the WGB are higher than those in the SGB within the wall-shear

403 layer  $0 < z \leq 0.2h$ , having a greater peak value in the former than in the latter. Nevertheless, the  $\langle I \rangle$   
 404 profiles in both the beds collapse above  $z = 0.2h$ . Therefore, it can be concluded that the WGB is  
 405 to enhance the turbulence level within the wall-shear layer owing to a higher roughness in the  
 406 WGB than in the SGB.  
 407

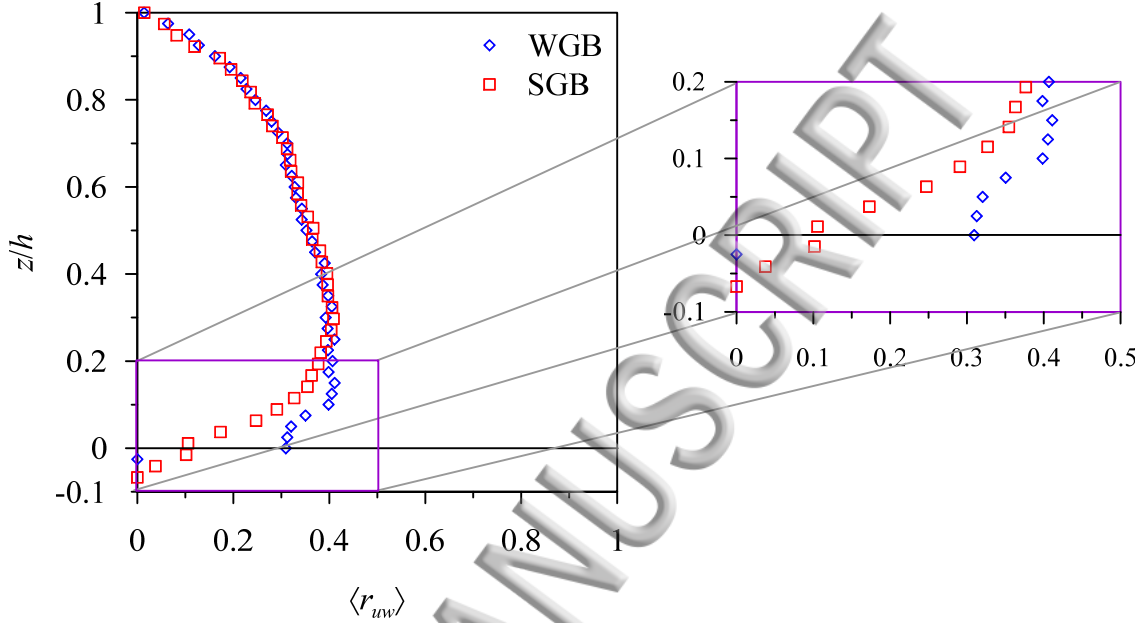


408  
 409  
 410 FIG. 9. Variations of the ratio of SA vertical and streamwise turbulent intensities  $\langle \sigma_w \rangle / \langle \sigma_u \rangle$  with  
 411 dimensionless vertical distance  $z/h$  in the WGB and SGB.  
 412

413 The degree of anisotropy can be assessed from the  $\langle \sigma_w \rangle / \langle \sigma_u \rangle$  ratio that performs as an anisotropy  
 414 indicator.<sup>61,62</sup> Here,  $\langle \sigma_u \rangle$  is the SA streamwise turbulence intensity, given by  $\langle \overline{u'u'} \rangle^{0.5}$ , and  $\langle \sigma_w \rangle$  is  
 415 the SA vertical turbulence intensity, given by  $\langle \overline{w'w'} \rangle^{0.5}$ . Figure 9 shows the variations of the  
 416  $\langle \sigma_w \rangle / \langle \sigma_u \rangle$  ratio with  $z/h$  ( $=0.1$  to  $1$ ) in the WGB and SGB. In addition, the variations are shown  
 417 in the inset in an enlarged frame up to the edge of the wall-shear layer ( $z/h = 0.2$ ). It is evident that  
 418 the anisotropies in both the beds increase up to the top edge of the respective form-induced  
 419 sublayers, in which the anisotropy in the WGB is greater than that in the SGB. It may be noted  
 420 that Padhi et al.<sup>45</sup> reported the extents of the form-induced sublayers in the WGB and SGB as  $z =$   
 421  $0.1h$  and  $0.125h$ , respectively. However, above the form-induced sublayers of both the beds, the  
 422  $\langle \sigma_w \rangle / \langle \sigma_u \rangle \approx 0.6$  indicates that the anisotropy remains almost invariant with  $z$ , as one goes toward  
 423 the free surface. The  $\langle \sigma_w \rangle / \langle \sigma_u \rangle$  profiles suggest that the  $\langle \sigma_w \rangle$  is much smaller than the  $\langle \sigma_u \rangle$ . In the  
 424 WGB near-bed flow zone, the  $\langle \sigma_w \rangle$  varies in the range  $0.2\langle \sigma_u \rangle - 0.5\langle \sigma_u \rangle$ , while in the SGB, the  $\langle \sigma_w \rangle$   
 425 varies within  $0.3\langle \sigma_u \rangle - 0.5\langle \sigma_u \rangle$ . The results are in conformity with those reported in Dey and Nath<sup>62</sup>  
 426 and Deshpande and Kumar.<sup>63</sup> On the contrary, Nezu and Nakagawa<sup>17</sup> believed that the  $\langle \sigma_w \rangle / \langle \sigma_u \rangle$   
 427 ratio is a universal constant as 0.55 for a hydraulically smooth flow. Later, Dey and Raikar<sup>61</sup>  
 428 reported  $\langle \sigma_w \rangle / \langle \sigma_u \rangle \approx 0.6$  for the weakly mobile flow. Different values of  $\langle \sigma_w \rangle / \langle \sigma_u \rangle$  obtained by  
 429 various researchers were due to dissimilar experimental conditions. It can be concluded that in the  
 430 near-bed flow zone, the anisotropy in the WGB declines more rapidly with the vertical distance

431 in the SGB. It is attributed to the WGB roughness that induces enhanced  $u'$  as compared to  
 432  $w'$ .

433  
 434 **VI. SPATIALLY-AVERAGED SECOND- AND THIRD-ORDER CORRELATIONS**  
 435

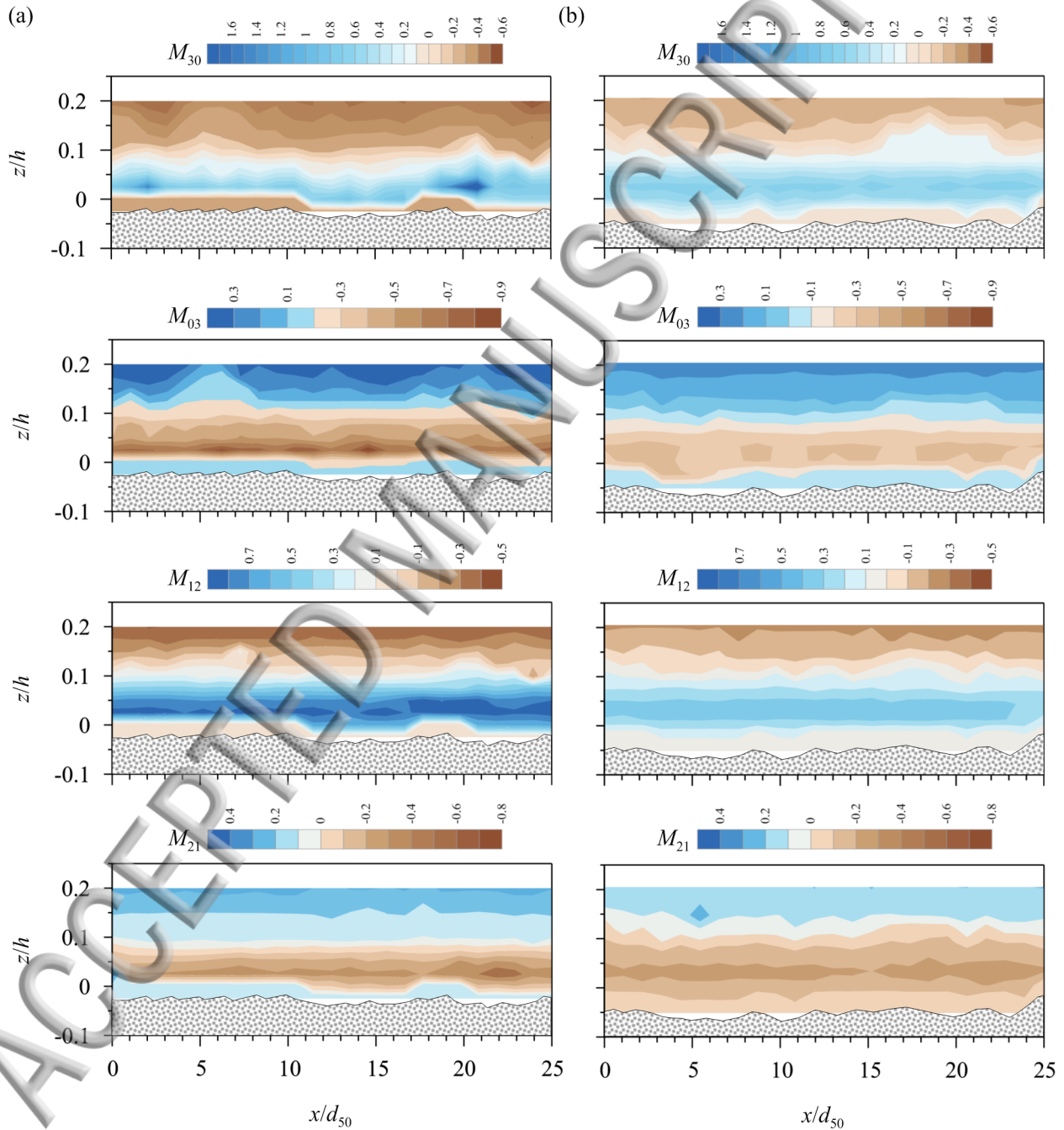


436  
 437  
 438 FIG. 10. Variations of SA second-order correlation  $\langle r_{uw} \rangle$  with dimensionless vertical distance  $z/h$   
 439 in the WGB and SGB.

440  
 441 The SA second-order correlation  $\langle r_{uw} \rangle$  indicates the degree of similarity of turbulence and is  
 442 represented as  $\langle r_{uw} \rangle = \langle u'w' \rangle / (\langle u'u' \rangle \langle w'w' \rangle)^{0.5}$ . Here,  $\langle u'w' \rangle$  is the SA RSS. Figure 10 represents the  
 443 variations of  $\langle r_{uw} \rangle$  with  $z/h$  ( $= -0.1$  to  $1$ ) in the WGB and SGB. In the inset, the variations are shown  
 444 up to  $z/h = 0.2$  in order to have their enlarged views in the wall-shear layer. It is evident that the  
 445  $\langle r_{uw} \rangle$  in the WGB increases up to the top edge of the wall-shear layer ( $z = 0.2h$ ) and then decreases,  
 446 as  $z$  increases further. Within the wall-shear layer, the  $\langle r_{uw} \rangle$  varies within  $0-0.4$  and diminishes  
 447 from  $0.4$  at  $z = 0.2h$  (at top of the wall-shear layer) to zero near the free surface. It implies that the  
 448 RSS plays a significant role in governing the  $\langle r_{uw} \rangle$  profile. Akin to the WGB, the  $\langle r_{uw} \rangle$  in the SGB  
 449 increases with an increase in  $z$  up to  $z = 0.3h$ . Thereafter, it follows almost the identical profile as  
 450 that in the WGB. To be specific, the  $\langle r_{uw} \rangle$  profiles in the WGB and SGB increase up to  $z = 0.2h$   
 451 and  $0.3h$ , signifying a thinner layer affected by roughness in the WGB. Another point is that the  
 452 magnitude of the  $\langle r_{uw} \rangle$  profile within this layer in the WGB is greater than that in the SGB.  
 453 Therefore, the Reynolds stresses exhibit a better correlation in the WGB than in the SGB.

454 The third-order correlations carry stochastic information about  $u'$  and  $w'$  in terms of transport  
 455 and diffusion of turbulent stresses. They can be linked to the turbulent coherent structures related  
 456 to the bursting events, due to the preservation of their signs. The third-order correlations  $M_{jk}$  can  
 457 be given by  $M_{jk} = \widehat{u}^j \widehat{w}^k$ ,<sup>58</sup> where  $\widehat{u} = u' / (\overline{u'u'})^{0.5}$  and  $\widehat{w} = w' / (\overline{w'w'})^{0.5}$  with  $j + k = 3$ . Depending on  
 458 the values of  $j$  and  $k$ , the third-order correlations are expressed as  $M_{30}$ ,  $M_{03}$ ,  $M_{12}$ , and  $M_{21}$ . Here,

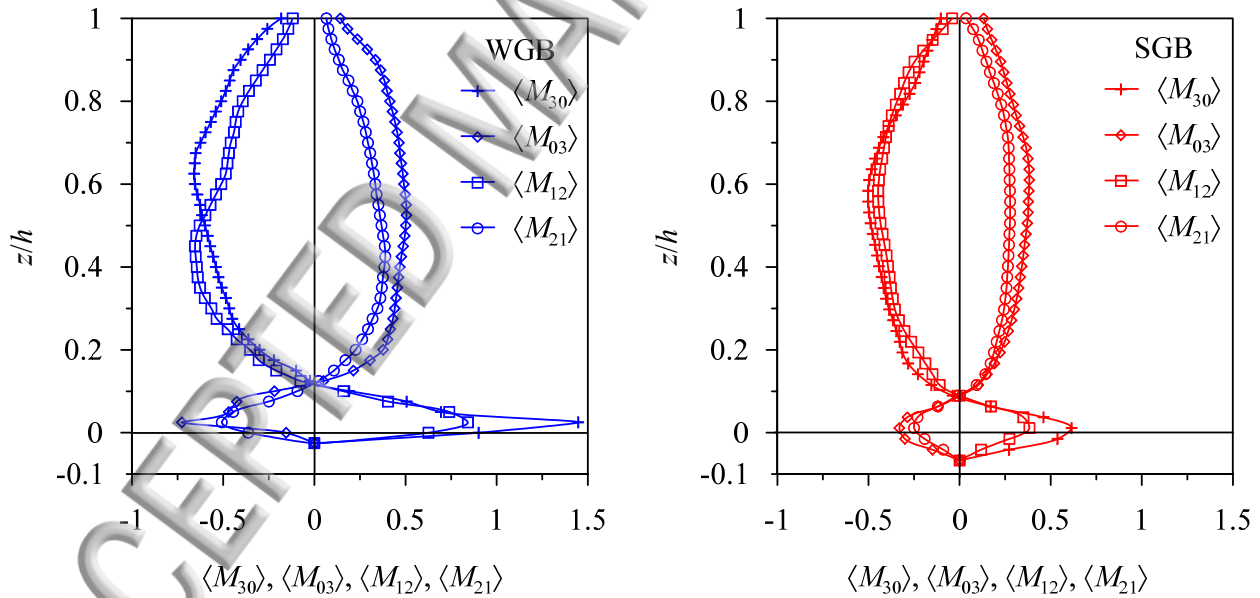
459  $M_{30}$  and  $M_{03}$  denote the streamwise and vertical skewness of temporal velocity fluctuations  $u'$  and  
 460  $w'$ , respectively. From the hydrodynamics viewpoint, the  $M_{30}$  ( $= \overline{\hat{u}^3}$ ) refers to the streamwise flux  
 461 of  $\overline{u'u'}$ , while the  $M_{03}$  ( $= \overline{\hat{w}^3}$ ) defines the vertical flux of  $\overline{w'w'}$ . On the other hand, the  $M_{12}$  ( $= \overline{\hat{u}\hat{w}^2}$   
 462 ) signifies the diffusion of  $\overline{w'w'}$  in the streamwise direction and the  $M_{21}$  ( $= \overline{\hat{u}^2\hat{w}}$ ) indicates the  
 463 diffusion of  $\overline{u'u'}$  in the vertical direction.<sup>3</sup>  
 464



465  
466

467 FIG. 11. Contours of time-averaged third-order correlations  $M_{jk}$  on a vertical central plane in the  
468 (a) WGB and (b) SGB.

469  
470 The contours of time-averaged third-order correlations  $M_{jk}$  on a vertical central plane in the  
471 WGB and SGB are illustrated in Figs. 11(a) and 11(b), respectively. In both the WGB and SGB,  
472 the streamwise distributions of  $M_{30}$  are positive in the near-bed flow zone, but negative in the upper  
473 spatial flow domain. On the other hand, the distributions of  $M_{03}$  are negative in the near-bed flow  
474 zone, but positive in the upper spatial flow domain. The combination of positive  $M_{30}$  and negative  
475  $M_{03}$  composes the sweeps, by transporting the  $\overline{u'u'}$  flux in the downstream direction and the  $\overline{w'w'}$   
476 flux in the downward direction. Conversely, the combination of negative  $M_{30}$  and positive  $M_{03}$   
477 forms the ejections, by transporting the  $\overline{u'u'}$  flux in the upstream direction and the  $\overline{w'w'}$  flux in the  
478 upward direction.<sup>42,64</sup> Further, in the WGB and SGB, the streamwise distributions of  $M_{12}$  and  $M_{21}$   
479 in the near-bed flow zone are positive and negative, respectively, while they are negative and  
480 positive in the away-bed spatial flow domain. The combination of positive  $M_{12}$  and negative  $M_{21}$   
481 refers to the diffusion of  $\overline{w'w'}$  in the downstream direction and  $\overline{u'u'}$  in the downward direction. On  
482 the contrary, the combination of negative  $M_{12}$  and positive  $M_{21}$  corresponds to the diffusion of  $\overline{w'w'}$   
483 in the upstream direction and  $\overline{u'u'}$  in the upward direction. Interestingly, the effects of bed  
484 topography on the  $M_{jk}$  contours are evident, because the  $M_{jk}$  contours near the bed follow similar  
485 profiles as the bed surface profiles in the WGB and SGB. However, the  $M_{jk}$  contours in the WGB  
486 are fairly uniform as compared to those in the SGB, because of the well-organized WGB roughness  
487 structure as compared to the randomly poised SGB roughness structure.  
488



489  $\langle M_{30} \rangle, \langle M_{03} \rangle, \langle M_{12} \rangle, \langle M_{21} \rangle$   
490  
491 FIG. 12. Variations of SA third-order correlations  $\langle M_{jk} \rangle$  with dimensionless vertical distance  $z/h$  in  
492 the WGB and SGB.

493  
494 Regarding the SA third-order correlations  $\langle M_{jk} \rangle$ , Fig. 12 depicts the variations of  $\langle M_{jk} \rangle$  with  $z/h$   
495 in the WGB and SGB. In both the beds, the  $\langle M_{30} \rangle$  and  $\langle M_{12} \rangle$  initiate with the positive values and  
496 attain their respective peaks just above the crest level at  $z = 0.025h$  and  $0.01h$  in the WGB and

497 SGB, respectively. Subsequently, the  $\langle M_{30} \rangle$  and  $\langle M_{12} \rangle$  start decreasing with an increase in  $z$ . In the  
 498 WGB, for  $z > 0.1h$  (just at the top edge of the form-induced sublayer), the  $\langle M_{30} \rangle$  and  $\langle M_{12} \rangle$  change  
 499 their signs, becoming negative for the rest of the vertical distance. Similar to the WGB, in the  
 500 SGB, the  $\langle M_{30} \rangle$  and  $\langle M_{12} \rangle$  change their signs at a vertical distance  $z = 0.09h$  (within the form-  
 501 induced sublayer), becoming negative for the rest of the vertical distance.

502 Unlike the  $\langle M_{30} \rangle$  and  $\langle M_{12} \rangle$  profiles, the  $\langle M_{03} \rangle$  and  $\langle M_{21} \rangle$  profiles in both the WGB and SGB  
 503 start with the negative values within the interfacial sublayer, which is the flow layer below the  
 504 crest within the interstices of gravels. In the WGB, the  $\langle M_{03} \rangle$  and  $\langle M_{21} \rangle$  reach their negative peaks  
 505 at  $z = 0.025h$ , while in the SGB, their peaks appear at  $z = 0.01h$ . Thereafter, both the  $\langle M_{03} \rangle$  and  
 506  $\langle M_{21} \rangle$  start decreasing with an increase in  $z$ . Akin to the  $\langle M_{30} \rangle$  and  $\langle M_{12} \rangle$  profiles, the  $\langle M_{03} \rangle$  and  
 507  $\langle M_{21} \rangle$  profiles change their signs at  $z = 0.1h$  in the WGB and  $0.09h$  in the SGB, becoming positive.

508 In conclusion, the analysis of the third-order correlations  $\langle M_{jk} \rangle$  reveals the role of bursting events  
 509 in different flow layers. The sweeps start dominating from the interfacial sublayer and extending  
 510 up to the form-induced sublayer ( $z = 0.09h$  and  $0.11h$  in the WGB and SGB, respectively). On the  
 511 other hand, there is a changeover of the bursting events above it and the ejections are prevalent in  
 512 the main flow layer. These results are directly correlated with the TKE fluxes and the conditional  
 513 RSS obtained by Padhi et al.<sup>45</sup> In essence, the roughness sublayer (the interfacial sublayer and the  
 514 majority of the form-induced sublayer) is governed by the arrival of rapidly moving fluid streaks.  
 515 Besides, comparison of the third-order correlations in both the beds infers that for a given vertical  
 516 distance, the profiles in the WGB have higher values than those in the SGB, because larger  
 517 temporal velocity fluctuations prevail in the WGB.

518

## 519 VII. TIME-AVERAGED AND SPATIALLY-AVERAGED TKE BUDGET

520

521 The TKE budget demonstrates the relative importance of physical processes that influence the  
 522 turbulent fluid motions. For a two-dimensional steady-uniform open-channel flow, the TKE  
 523 budget equation can be expressed as

524

$$525 \underbrace{\overline{u'w'}}_{t_p} \frac{\partial \bar{u}}{\partial z} = \varepsilon + \underbrace{\frac{\partial f_{kw}}{\partial z}}_{t_d} + \underbrace{\frac{1}{\rho} \frac{\partial \overline{p'w'}}{\partial z}}_{p_d} - \underbrace{\nu \frac{\partial^2 k}{\partial z^2}}_{\nu_d} \quad (2)$$

526

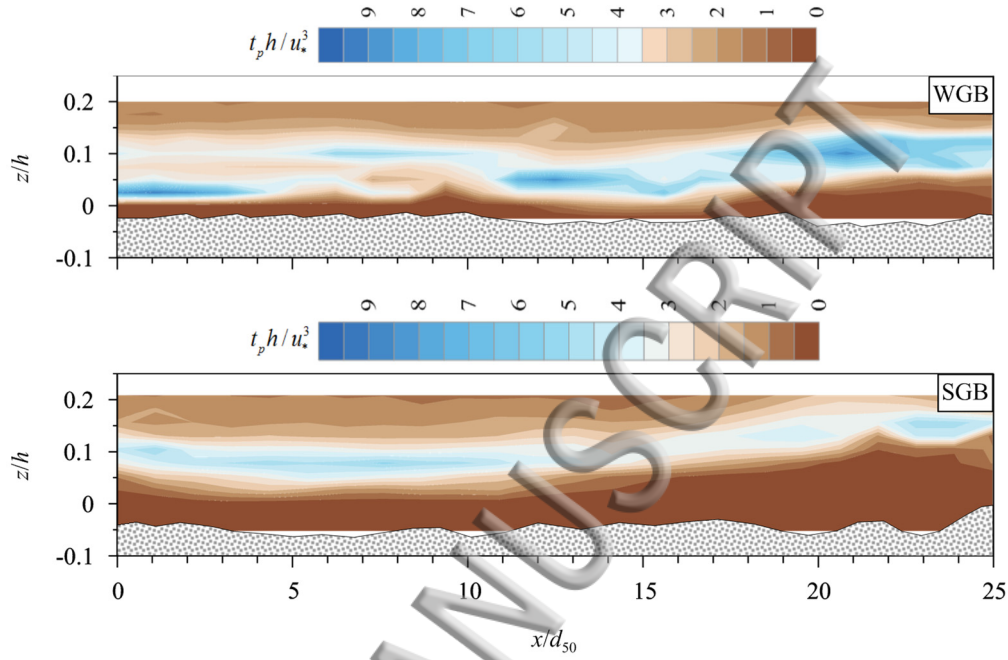
527 where  $t_p$  is the TKE production rate,  $\varepsilon$  is the TKE dissipation rate,  $t_d$  is the TKE diffusion rate,  $p_d$   
 528 is the pressure energy diffusion rate,  $\nu_d$  is the viscous diffusion rate,  $f_{kw}$  is the vertical TKE flux,  
 529 and  $p'$  is the pressure fluctuation. The term  $\nu_d$  can be neglected, because it has minimal contribution  
 530 to the TKE budget in a rough flow. In a two-dimensional PIV system, the implication of two-  
 531 dimensionality involves in approximation of  $f_{kw}$  as  $f_{kw} = 0.75(\overline{u'u'w'} + \overline{w'w'w'})$ .<sup>58</sup> It is pertinent to  
 532 mention that the bed roughness elements create a strong fluid mixing. As a result, the  $t_p$  becomes  
 533 higher than the  $\varepsilon$  and the transport of TKE occurs in an upward and downward directions through  
 534 the  $t_d$  and  $p_d$ .<sup>65,66</sup> However, the  $t_p$ ,  $\varepsilon$ , and  $t_d$  can be estimated directly from the experimental data.  
 535 Hence, the  $p_d$  can be calculated as a residue ( $p_d = t_p - \varepsilon - t_d$ ).<sup>42,67,68</sup>

536 To determine the TKE dissipation rate  $\varepsilon$ , the expression given by Fincham et al.<sup>69</sup> was used in  
 537 this study. It is

538

$$\varepsilon = \frac{15}{7} \nu \left[ 2 \left( \frac{\partial u'}{\partial x} \right)^2 + 2 \left( \frac{\partial w'}{\partial z} \right)^2 + \left( \frac{\partial u'}{\partial z} \right)^2 + \left( \frac{\partial w'}{\partial x} \right)^2 + 2 \left( \frac{\partial u'}{\partial z} \frac{\partial w'}{\partial x} \right) \right]. \quad (3)$$

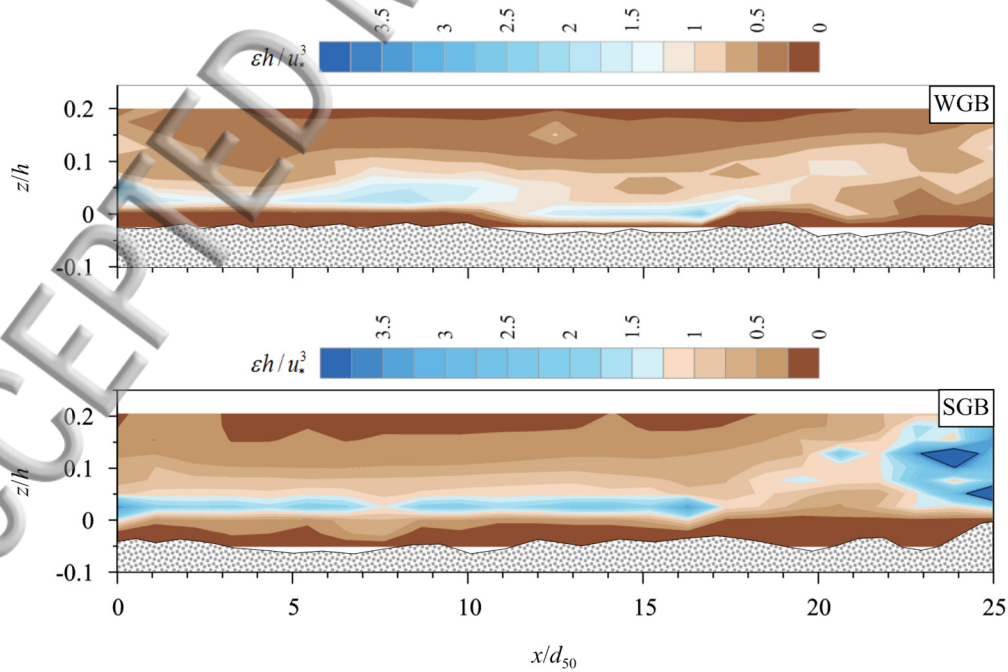
540



541

542

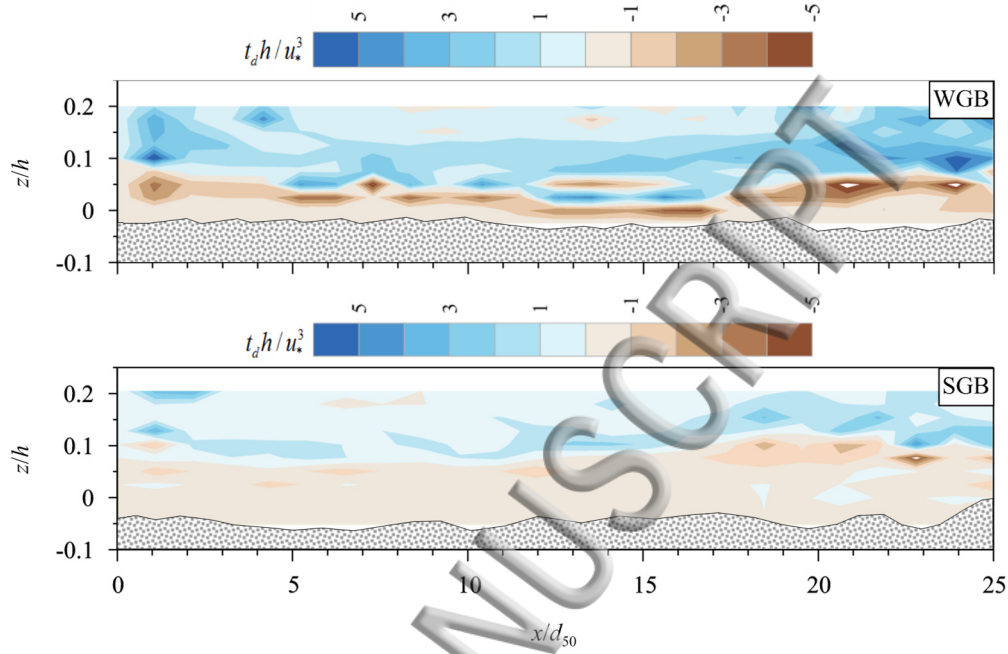
543 FIG. 13. Contours of dimensionless time-averaged TKE production rate  $t_p h / u_*^3$  on a vertical central  
544 plane in the WGB and SGB.  
545



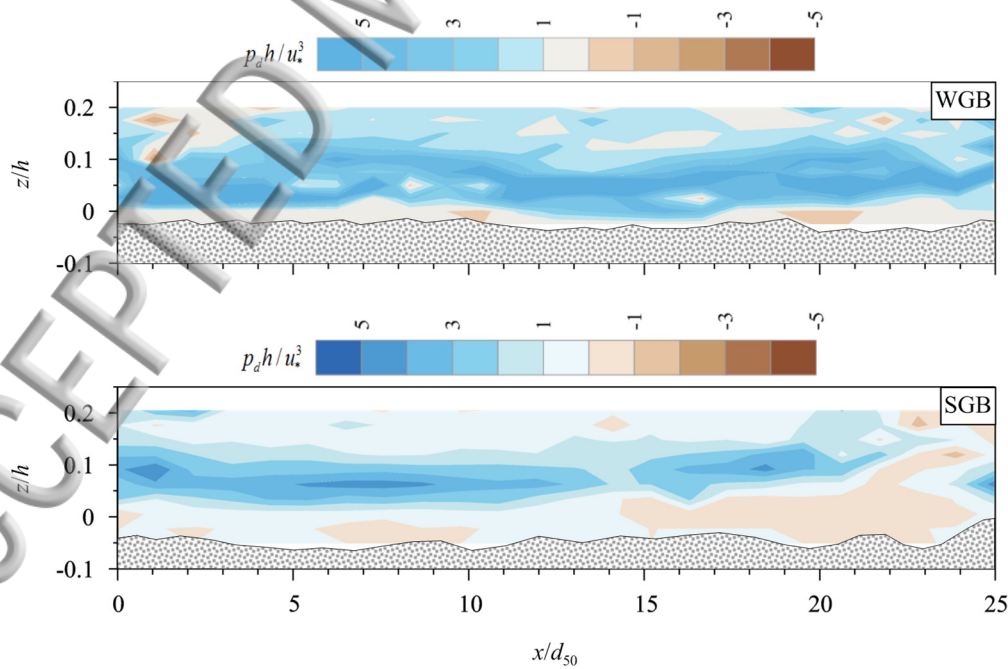
546

547

548 FIG. 14. Contours of dimensionless TKE dissipation rate  $\varepsilon h/u_*^3$  on a vertical central plane in the  
 549 WGB and SGB.  
 550



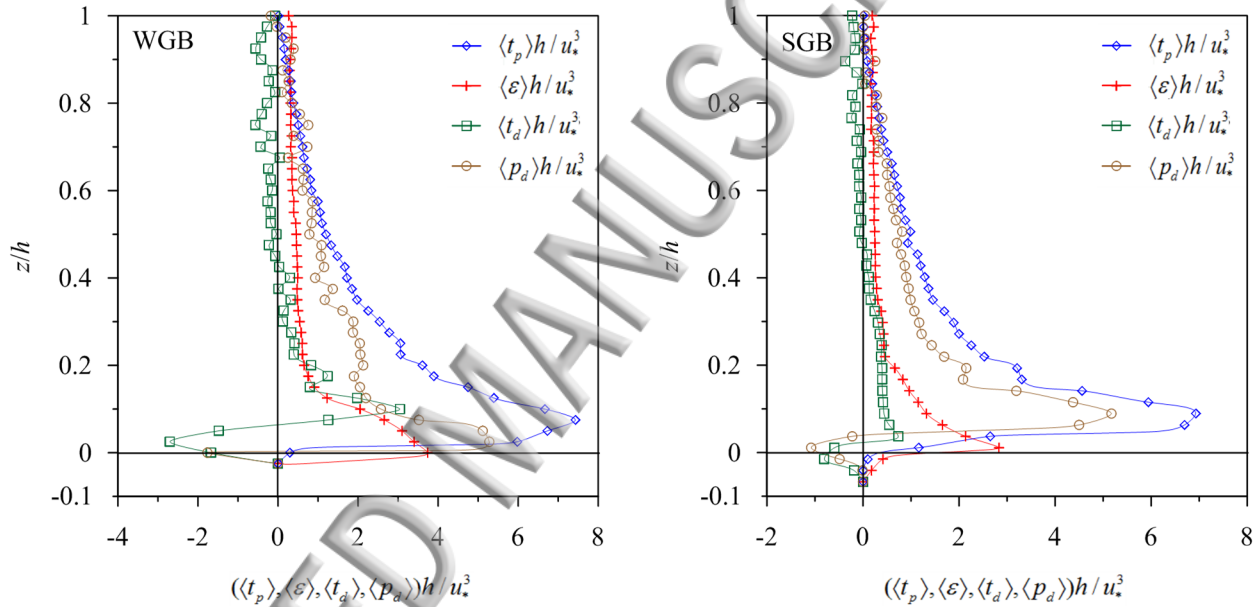
551  
 552  
 553 FIG. 15. Contours of dimensionless time-averaged TKE diffusion rate  $t_d h/u_*^3$  on a vertical central  
 554 plane in the WGB and SGB.  
 555



556  
 557

558 FIG. 16. Contours of dimensionless time-averaged pressure energy diffusion rate  $p_d h / u_*^3$  on a  
559 vertical central plane in the WGB and SGB.  
560

561 Figures 13–16 present the contours of dimensionless TKE production rate  $t_p h / u_*^3$ , TKE  
562 dissipation rate  $\varepsilon h / u_*^3$ , TKE diffusion rate  $t_d h / u_*^3$ , and pressure energy diffusion rate  $p_d h / u_*^3$  on a  
563 vertical central plane in the WGB and SGB. The spatial flow domains are restricted to the wall-  
564 shear layer portion ( $z \leq 0.20h$ ) to highlight the bed roughness influenced flow fields in the context  
565 of TKE budget terms. The streamwise distributions of the TKE budget terms clearly exemplify the  
566 influence of the WGB and SGB bed roughness structures. Over all, in the WGB having higher  
567 roughness, the individual TKE budget terms exhibit a spatially quasi-periodic distribution, while  
568 in the SGB, they display a spatially quasi-homogeneous distribution.  
569



570  
571  
572 FIG. 17. Variations of dimensionless SA TKE budget terms (production rate, dissipation rate,  
573 dispersive diffusion rate, and pressure energy diffusion rate) with dimensionless vertical distance  
574  $z/h$  in the WGB and SGB.  
575

576 In order to have a summarized picture of the TKE budget terms, the variations of dimensionless  
577 SA TKE budget terms with  $z/h$  in the WGB and SGB are demonstrated in Fig. 17. From the  
578 dimensionless SA TKE production rate  $\langle t_p \rangle h / u_*^3$  profiles, it is evident that in both the beds, the  $\langle t_p \rangle$   
579 profiles initiate from the interfacial sublayer and grow with an increase in vertical distance  $z$ . They  
580 attain their respective peaks at the top edge of the form-induced sublayer and then decrease, as  $z$   
581 further increases. The results are in conformity with those reported in Mignot et al.<sup>40</sup> and Dey and  
582 Das.<sup>42</sup> Near the crest, the velocity gradient attains its peak, which aids to maximize the TKE  
583 production rate. Moreover, the fluid mixing is triggered by gravels. As a result, the temporal  
584 velocity fluctuations increase and so does the RSS. Further, it is discernable from Fig. 17 that for

585 a given  $z$ , the  $\langle t_p \rangle h / u_*^3$  has a larger magnitude in the WGB than in the SGB. The underlying reason  
586 is attributed to the higher WGB roughness than the SGB, which causes to enhance the temporal  
587 velocity fluctuations in the WGB.<sup>17,45</sup>

588 An examination of dimensionless SA TKE dissipation rate  $\langle \varepsilon \rangle h / u_*^3$  profiles demonstrates that  
589 in both the beds, the  $\langle \varepsilon \rangle$  profiles reach their peak values at the crest. Thereafter, they decrease, as  
590 one moves toward the free surface. Interestingly, within the wall-shear layer ( $z \leq 0.2h$ ), the  $\langle \varepsilon \rangle$   
591 profiles diminish rapidly as compared to those in the outer flow layer. Similar results were also  
592 reported in Mignot et al.<sup>40</sup> and Manes et al.<sup>70</sup> Comparing the magnitudes of  $\langle \varepsilon \rangle$  in both the beds, it  
593 is found that for a given  $z$ , the  $\langle \varepsilon \rangle$  attains a higher value in the WGB than in the SGB. According  
594 to Dey and Das,<sup>42</sup> Padhi et al.<sup>45</sup> and Sarkar et al.,<sup>64</sup> the bed roughness height is directly associated  
595 to the temporal velocity fluctuations resulting in an enhanced  $\langle \varepsilon \rangle$ . In this study, the higher  
596 roughness in the WGB than in the SGB causes an increase in streamwise temporal velocity  
597 fluctuations in the former than in the latter.

598 From the dimensionless SA TKE diffusion rate  $\langle td \rangle h / u_*^3$  profiles, it is noticeable that in both the  
599 beds, the  $\langle td \rangle$  profiles that initiate from the interfacial sublayer, being negative, gradually increase  
600 (absolute magnitudes) with an increase in  $z$ , attaining their negative peaks just above the crest.  
601 Then, they gradually decrease, as  $z$  increases further. In the WGB, the  $\langle td \rangle$  changes its sign,  
602 becoming positive near the top edge of the form-induced sublayer, while in the SGB, it changes  
603 sign below the form-induced sublayer. With a further increase in  $z$ , the  $\langle td \rangle$  profiles attain their  
604 positive peak just above the roughness layer and thereafter, they start to diminish. They again  
605 change their sign well above the wall-shear layer ( $z = 0.4h$ ), becoming negative for the rest of the  
606 vertical distance. Negative  $\langle td \rangle$  signifies a gain in the TKE production rate. Sarkar et al.<sup>64</sup> also had  
607 a similar observation. At a given  $z$ , the difference between the  $\langle td \rangle$  magnitudes in the WGB and  
608 SGB is ascribed to the difference in the temporal velocity fluctuations in both the beds.

609 The dimensionless SA pressure energy diffusion rate  $\langle pd \rangle h / u_*^3$  profiles reveal that in both the  
610 beds, the  $\langle pd \rangle$  profiles start from the interfacial sublayer, being negative, attaining their negative  
611 peaks in the WGB at the crest and in the SGB above the crest. Thereafter, they decrease (absolute  
612 magnitudes) sharply becoming positive above the crest. The positive peaks of  $\langle pd \rangle$  attain at  $z =$   
613  $0.04h$  in the WGB and at  $z = 0.1h$  in the SGB. Then, the  $\langle pd \rangle$  profiles decline, as one moves toward  
614 the free surface. Negative  $\langle pd \rangle$  suggests a gain in the TKE production rate.<sup>42,64,71</sup> It is noticeable  
615 that in the near-bed flow zone, the lag between the  $\langle t_p \rangle$  and the  $\langle \varepsilon \rangle$  is narrowed down, resulting in  
616 a negative  $\langle pd \rangle$ . Akin to other SA TKE budget terms, at a given  $z$  in the near-bed flow zone, the  
617  $\langle pd \rangle$  is greater in the WGB than in the SGB. It can be concluded that the WGB induces a near-bed  
618 low-pressure (negative) flow zone, while the SGB produces a near-bed positive pressure flow  
619 zone.

620

## 621 VIII. CONCLUDING REMARKS

622

623 The impact of gravel-bed induced coherent structures on the near-bed time-averaged flow  
624 structures is studied measuring the instantaneous flow velocity by a two-dimensional PIV system  
625 in the WGB and SGB, keeping the flow identical. The key findings of this study are summarized  
626 as follows:

627 The WGB possesses an organized bed roughness structure due to the action of water-work,  
628 while the SGB roughness structure is randomly poised. The roughness height is found to be higher  
629 in the WGB than in the SGB. The analysis of instantaneous velocity vectors and contours in the  
630 WGB and SGB infers that the motions of the fluid streaks are repetitive in nature with time. In the  
631 near-bed flow zone, the velocity vectors in the WGB are less scattered than those in the SGB,  
632 because the roughness structure is organized in the WGB. In the WGB and SGB, the near-bed  
633 vorticity fields show the clockwise and counterclockwise motions of the flow vortices, which  
634 cause the streamwise flow to decelerate and accelerate, respectively.

635 The SA turbulence indicator in the WGB and SGB infers that the turbulence level is relatively  
636 high in the near-bed flow zone, because the bed roughness elements cause the turbulence  
637 production. However, as the vertical distance increases, the turbulence level dampens gradually.  
638 The comparative study suggests that near the crest, the turbulence level in the WGB is higher than  
639 that in the SGB, due to the higher roughness in the former than in the latter. Notably, the higher  
640 roughness can produce higher temporal velocity fluctuations.

641 Further, in the near-bed flow zone, the second- and third-order correlations for a given vertical  
642 distance possess higher magnitudes in the WGB than in the SGB. In both the beds, the third-order  
643 correlations also reveal that the sweeps are the dominant events in the near-bed flow zone, with a  
644 downstream diffusion of vertical normal stress and a downward diffusion of streamwise normal  
645 stress. Conversely, the ejections are the governing mechanism in the outer flow layer with an  
646 upstream diffusion of vertical normal stress and an upward diffusion of streamwise normal stress.

647 In the SA TKE budget, all of the budget terms in the WGB reach their respective peaks at or  
648 above the crest level. On the contrary, in the SGB, the SA TKE production rate and the pressure  
649 energy diffusion rate reach their respective peaks above the crest. Comparative study reveals that  
650 for a given vertical distance, all the DA TKE budget terms in the WGB have higher magnitudes  
651 than those in the SGB in the near-bed flow zone.

652 In essence, this study provides an insight into the near-bed turbulent flow and vorticity  
653 structures in the WGB and SGB. Analysis of the near-bed flow fields enables us to comprehend  
654 the effects of the bed roughness structures on the turbulence characteristics in the WGB and SGB  
655 flows. The comparison of the results reveals that the SGB causes an underestimation of the  
656 magnitudes of turbulence parameters than the WGB, which closely resemblances a natural gravel-  
657 bed river. Therefore, it is prudent to perform the laboratory experimental studies in a WGB, rather  
658 than an SGB, in order to obtain the turbulence characteristics close to those obtained in a natural  
659 watercourse.

660

## 661 **ACKNOWLEDGEMENTS**

662

663 The first author is thankful to the University of Calabria, Italy for the invitation to work in the  
664 *Laboratorio "Grandi Modelli Idraulici"*. The work was partially funded by the JC Bose Fellowship  
665 project (JBD).

666

## 667 **List of symbols:**

668

669	$B$	flume width
670	$d_{50}$	median size of gravel
671	$Fr$	flow Froude number
672	$f_{kw}$	vertical turbulent kinetic energy flux

674	$n$	gravitational acceleration
675	$I$	flow depth
676	$\langle I \rangle$	turbulence indicator
677	$k$	spatially-averaged turbulence indicator
678	$\langle k \rangle$	turbulent kinetic energy
679	$l_x$	spatially-averaged turbulent kinetic energy
680	$M_{jk}$	sampling length in streamwise direction
681	$\langle M_{jk} \rangle$	third-order correlations
682	$N$	spatially-averaged third-order correlations
683	$n$	total number of points in streamwise direction
684	$p'$	number of points in streamwise direction
685	$pd$	pressure fluctuation
686	$\langle pd \rangle$	pressure energy diffusion rate
687	$Q$	spatially-averaged pressure energy diffusion rate
688	$\langle r_{uw} \rangle$	flow discharge
689	$R$	spatially-averaged second-order correlation
690	$R^*$	flow Reynolds number
691	$R_{lx}$	shear Reynolds number
692	$t$	autocorrelation function
693	$t_d$	time
694	$\langle t_d \rangle$	turbulent kinetic energy diffusion rate
695	$t_p$	spatially-averaged turbulent kinetic energy diffusion rate
696	$\langle t_p \rangle$	turbulent kinetic energy production rate
697	$U_{avg}$	spatially-averaged turbulent kinetic energy production rate
698	$U_c$	average flow velocity
699	$\bar{U}$	critical flow velocity for initiation of gravel motion
700	$\langle \bar{U} \rangle$	time-averaged flow velocity
701	$u, w$	double-averaged flow velocity
702	$u', w'$	instantaneous streamwise and vertical velocity components, respectively
703	$\langle u'w' \rangle$	fluctuations of streamwise and vertical velocity components, respectively
704	$\bar{u}, \bar{w}$	spatially-averaged Reynolds shear stress
705	$\langle \bar{u} \rangle, \langle \bar{w} \rangle$	time-averaged streamwise and vertical velocity components, respectively
706	$u^*$	double-averaged streamwise and vertical velocity components, respectively
707	$\nu_d$	shear velocity
708	$x, z$	viscous diffusion rate
709	$z'$	streamwise and vertical distances, respectively
710	$\Delta$	bed surface fluctuation with respect mean surface elevation
711	$\Delta_k$	submerged relative density of gravel
712	$\Delta t$	average roughness height
713	$\delta x$	time scale
714	$\varepsilon$	sampling interval
715	$\langle \varepsilon \rangle$	turbulent kinetic energy dissipation rate
716	$\lambda_x$	spatially-averaged turbulent kinetic energy dissipation rate
		horizontal length scale of bed surface fluctuations

718  $\langle \sigma_u \rangle, \langle \sigma_w \rangle$  kinematic viscosity of water  
 719  $\omega$  spatially-averaged streamwise and vertical turbulence intensities, respectively  
 720  $\bar{\omega}$  instantaneous vorticity  
 721 time-averaged vorticity

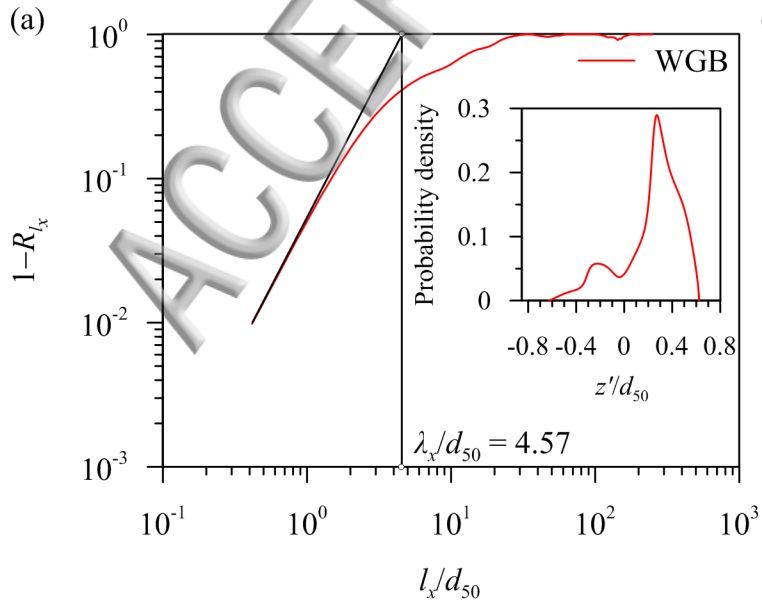
- 722 <sup>1</sup> A. G. Roy, T. Buffin-Bélanger, H. Lamarre, and A. D. Kirkbride, “Size, shape and dynamics of  
 723 large-scale turbulent flow structures in a gravel-bed river,” *J. Fluid Mech.* **500**, 1–27 (2004).  
 724 <sup>2</sup> R. J. Adrian and I. Marusic, “Coherent structures in flow over hydraulic engineering surfaces.” *J.*  
 725 *Hydraul. Res.* **50**, 451–464 (2012).  
 726 <sup>3</sup> S. Dey, *Fluvial Hydrodynamics: Hydrodynamic and Sediment Transport Phenomena* (Springer-  
 727 Verlag, Berlin, Germany, 2014).  
 728 <sup>4</sup> S. J. Kline, W. C. Reynolds, R. A. Schraub, and P. W. Runstadler, “The structure of turbulent  
 729 boundary layers,” *J. Fluid Mech.* **30**, 741–773 (1967).  
 730 <sup>5</sup> R. E. Falco, “Coherent motions in the outer region of turbulent boundary layers,” *Phys. Fluids*  
 731 **20**, S124–S132 (1977).  
 732 <sup>6</sup> B. J. Cantwell, “Organized motion in turbulent flow,” *Annu. Rev. Fluid Mech.* **13**, 457–515  
 733 (1981).  
 734 <sup>7</sup> A. K. M. F. Hussain, “Coherent structures—reality and myth,” *Phys. Fluids* **26**, 2816–2850 (1983).  
 735 <sup>8</sup> R. J. Adrian and P. Moin, “Stochastic estimation of organized turbulent structure: Homogeneous  
 736 shear flow,” *J. Fluid Mech.* **190**, 531–559 (1988).  
 737 <sup>9</sup> J. Kim, S. J. Kline, and W. C. Reynolds, “The production of turbulence near a smooth wall in a  
 738 turbulent boundary layer,” *J. Fluid Mech.* **50**, 133–160 (1971).  
 739 <sup>10</sup> J. Kim, P. Moin, and R. Moser, “Turbulence statistics in fully developed channel flow at low  
 740 Reynolds number,” *J. Fluid Mech.* **177**, 133–166 (1987).  
 741 <sup>11</sup> J. Zhou, R. J. Adrian, and S. Balachandar, “Autogeneration of near-wall vortical structures in  
 742 channel flow,” *Phys. Fluids* **8**, 288–290 (1996).  
 743 <sup>12</sup> R. Adrian, K. Christensen, and Z. Liu, “Analysis and interpretation of instantaneous turbulent  
 744 velocity fields,” *Exp. Fluids* **29**, 275–290 (2000).  
 745 <sup>13</sup> R. J. Adrian, C. D. Meinhart, and C. D. Tomkins, “Vortex organization in the outer region of the  
 746 turbulent boundary layer,” *J. Fluid Mech.* **422**, 1–54 (2000).  
 747 <sup>14</sup> A. J. Grass, “Structural features of turbulent flow over smooth and rough boundaries,” *J. Fluid*  
 748 *Mech.* **50**, 233–255 (1971).  
 749 <sup>15</sup> T. G. Drake, R. L. Shreve, W. E. Dietrich, and P. J. Whiting, “Bedload transport of fine gravel  
 750 observed by motion-picture photography,” *J. Fluid Mech.* **192**, 193–217 (1988).  
 751 <sup>16</sup> A. J. Grass, R. J. Stuart, and M. Mansour-Tehrani, “Vortical structures and coherent motion in  
 752 turbulent flow over smooth and rough boundaries,” *Philos. Trans. R. Soc. London A* **336**, 35–  
 753 65 (1991).  
 754 <sup>17</sup> I. Nezu and H. Nakagawa, *Turbulence in Open-Channel Flows* (International Association of  
 755 Hydraulic Engineering and Research Monograph, Rotterdam, The Netherlands, 1993).  
 756 <sup>18</sup> C. Manes, L. Ridolfi, and G. Katul, “A phenomenological model to describe turbulent friction  
 757 in permeable-wall flows,” *Geophys. Res. Lett.* **39**, L14403 (2012).  
 758 <sup>19</sup> M. P. Lamb, F. B. Brian, and M. Fuller, “Hydrodynamics of steep streams with planar coarse-  
 759 grained beds: Turbulence, flow resistance, and implications for sediment transport,” *Water*  
 760 *Resour. Res.* **53**, 2240–2263 (2017).

- 762 J. Voermans, M. Ghisalberti, and G. N. Ivey, “The variation of flow and turbulence across the  
763 sediment-water interface,” *J. Fluid Mech.* **824**, 413–437 (2017).
- 764 <sup>21</sup> M. R. Raupach, J. J. Finnigan, and Y. Brunet, “Coherent eddies and turbulence in vegetation  
765 canopies: the mixing layer analogy,” *Boundary-Layer Met.* **78**, 351–382 (1996).
- 766 <sup>22</sup> M. Ghisalberti and H. M. Nepf, “Mixing layers and coherent structures in vegetated aquatic  
767 flows,” *J. Geophys. Res. Oceans* **107**, 3011 (2002).
- 768 <sup>23</sup> I. Nezu and M. Sanjou, “Turbulence structure and coherent motion in vegetated canopy open-  
769 channel flows,” *J. Hydro-environ. Res.* **2**, 62–90 (2008).
- 770 <sup>24</sup> B. N. Bailey and R. Stoll, “The creation and evolution of coherent structures in plant canopy  
771 flows and their role in turbulent transport,” *J. Fluid Mech.* **789**, 425–460 (2016).
- 772 <sup>25</sup> N. Cagney and S. Balabani, “Lagrangian structures and mixing in the wake of a streamwise  
773 oscillating cylinder,” *Phys. Fluids* **28**, 045107 (2016).
- 774 <sup>26</sup> K. Fukuda, R. Balachandar, and R. M. Barron, “Development of vortex structures in the wake  
775 of a sharp-edged bluff body,” *Phys. Fluids* **29**, 125103 (2017).
- 776 <sup>27</sup> G. Riches, R. Martinuzzi, and C. Morton, “Proper orthogonal decomposition analysis of a  
777 circular cylinder undergoing vortex-induced vibrations,” *Phys. Fluids* **30**, 105103 (2018).
- 778 <sup>28</sup> J. M. Nelson, R. L. Shreve, and S. R. McLean, “Role of near-bed turbulence structure in bed  
779 load transport and bed form mechanics,” *Water Resour. Res.* **31**, 2071–2086 (1995).
- 780 <sup>29</sup> B. O. Santos, M. J. Franca, and R. M. L. Ferreira, “Coherent structures in open channel flows  
781 with bedload transport over a hydraulically rough bed,” in *Proceedings of International  
782 Conference on Fluvial Hydraulics, River Flow* (Laussane, Switzerland, 2014), pp. 883–890.
- 783 <sup>30</sup> C. J. Keylock, S. N. Lane, and K. S. Richards, “Quadrant/octant sequencing and the role of  
784 coherent structures in bed load sediment entrainment,” *J. Geophys. Res. Earth Surface* **119**,  
264–286 (2014).
- 785 <sup>31</sup> D. Hurther, U. Lemmin, and E. A. Terray, “Turbulent transport in the outer region of rough-wall  
786 open-channel flows,” *J. Fluid Mech.* **574**, 465–493 (2007).
- 787 <sup>32</sup> R. J. Hardy, J. L. Best, S. N. Lane, and P. E. Carbonneau, “Coherent flow structures in a depth-  
788 limited flow over a gravel surface: the role of near-bed turbulence and influence of Reynolds  
789 number,” *J. Geophys. Res. Earth Surface* **114**, 1–18 (2009).
- 790 <sup>33</sup> M. Detert, V. Nikora, and G. H. Jirka, “Synoptic velocity and pressure fields at the water-  
791 sediment interface of streambeds,” *J. Fluid Mech.* **660**, 55–86 (2010).
- 792 <sup>34</sup> M. Guala, C. D. Tomkins, K. T. Christensen, and R. J. Adrian, “Vortex organization in a  
793 turbulent boundary layer overlying sparse roughness elements,” *J. Hydraul. Res.* **50**, 465–481  
794 (2012).
- 795 <sup>35</sup> J. J. Voermans, M. Ghisalberti, and G. N. Ivey, “The hydrodynamic response of the sediment-  
796 water interface to coherent turbulent motions,” *Geophys. Res. Lett.* **45**, 10520–10527 (2018).
- 797 <sup>36</sup> T. Buffin-Bélanger, A. G. Roy, H. Lamarre, and A. D. Kirkbride, “On large-scale flow structures  
798 in a gravel-bed river,” *Geomorphology* **32**, 417–435 (2000).
- 799 <sup>37</sup> V. Nikora, K. Koll, I. McEwan, S. McLean, and A. Dittrich, “Velocity distribution in the  
800 roughness layer of rough-bed flows,” *J. Hydraul. Eng.* **130**, 1036–1042 (2004).
- 801 <sup>38</sup> V. Nikora, S. McLean, S. Coleman, D. Pokrajac, I. McEwan, L. Campbell, J. Aberle, D. Clunie,  
802 and K. Koll, “Double-averaging concept for rough-bed open-channel and overland flows:  
803 Applications,” *J. Hydraul. Eng.* **133**, 884–895 (2007).
- 804 <sup>39</sup> D. Pokrajac, I. McEwan, and V. Nikora, “Spatially averaged turbulent stress and its  
805 partitioning,” *Exp. Fluids* **45**, 73–83 (2008).

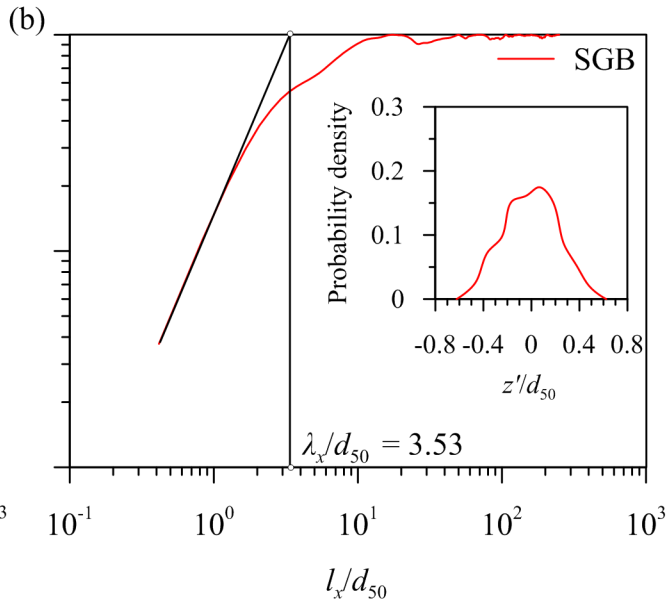
- 807 E. Mignot, E. Barthelemy, and D. Hurther, “Double-averaging analysis and local flow  
808 characterization of near-bed turbulence in gravel-bed channel flows,” *J. Fluid Mech.* **618**,  
809 279–303 (2009).
- 810 <sup>41</sup> S. Dey, S. Sarkar, and F. Ballio, “Double-averaging turbulence characteristics in seeping rough-  
811 bed streams,” *J. Geophys. Res. Earth Surface* **116**, F03020 (2011).
- 812 <sup>42</sup> S. Dey and R. Das, “Gravel-bed hydrodynamics: Double-averaging approach,” *J. Hydraul. Eng.*  
813 **138**, 707–725 (2012).
- 814 <sup>43</sup> D. Ferraro, S. Servidio, V. Carbone, S. Dey, and R. Gaudio, “Turbulence laws in natural bed  
815 flows,” *J. Fluid Mech.* **798**, 540–571 (2016).
- 816 <sup>44</sup> J. R. Cooper and S. J. Tait, “Water-worked gravel beds in laboratory flumes—a natural  
817 analogue?,” *Earth Surf. Processes Landforms* **34**, 384–397 (2009).
- 818 <sup>45</sup> E. Padhi, N. Penna, S. Dey, and R. Gaudio, “Hydrodynamics of water-worked and screeded  
819 gravel beds: A comparative study,” *Phys. Fluids* **30**, 085105 (2018).
- 820 <sup>46</sup> J. Aberle and V. Nikora, “Statistical properties of armored gravel bed surfaces,” *Water Resour.*  
821 *Res.* **42**, W11414 (2006).
- 822 <sup>47</sup> E. Padhi, N. Penna, S. Dey, and R. Gaudio, “Spatially averaged dissipation rate in flows over  
823 water-worked and screeded gravel beds,” *Phys. Fluids* **30**, 125106 (2018).
- 824 <sup>48</sup> J. L. Lumley and J. F. McMahon, “Reducing water tunnel turbulence by means of a honeycomb,”  
825 *J. Basic Eng.* **89**, 764–770 (1967).
- 826 <sup>49</sup> R. Loehrke and H. Nagib, “Reducing water tunnel turbulence by means of a honeycomb,” *J.*  
827 *Fluids Eng.* **98**, 342–351 (1976).
- 828 <sup>50</sup> L. R. Andersson, I. A. S. Larsson, J. G. I. Hellström, P. Andreasson, A. G. Andersson, and T. S.  
829 Lundström, “Characterization of flow structures induced by highly rough surface using  
830 particle image velocimetry, proper orthogonal decomposition and velocity correlations,”  
831 *Engineering* **10**, 399–416 (2018).
- 832 <sup>51</sup> C. R. Neill, “Mean-velocity criterion for scour of coarse uniform bed material,” in *Proceedings*  
833 *of International Association of Hydraulic Research 12th Congress* (Fort Collins, Colorado,  
834 1967), Vol. 1, pp. 46–54.
- 835 <sup>52</sup> S. K. Robinson, “Coherent motions in the turbulent boundary layers,” *Annu. Rev. Fluid Mech.*  
836 **23**, 601–639 (1991).
- 837 <sup>53</sup> C. R. Smith, “Coherent flow structures in smooth-wall turbulent boundary layers: Facts,  
838 mechanisms and speculation,” in *Coherent flow Structures in Open Channels*, edited by P.  
839 Ashworth, S. Bennett, J. L. Best, and S. McLelland (John Wiley & Sons, Chichester, UK,  
840 1996), pp. 804–813.
- 841 <sup>54</sup> C. Diaz-Daniel, S. Laizet, and J. C. Vassilicos, “Wall shear stress fluctuations: Mixed scaling  
842 and their effects on velocity fluctuations in a turbulent boundary layer,” *Phys. Fluids* **29**,  
843 055102 (2017).
- 844 <sup>55</sup> R. J. Adrian, “Structure of turbulent boundary layers,” in *Coherent Flow Structures at Earth’s*  
845 *Surface*, edited by J. G. Venditti, J. L. Best, M. Church, and R. J. Hardy (John Wiley & Sons,  
846 Chichester, UK, 2013), pp. 17–24.
- 847 <sup>56</sup> M. Lagha, “A comprehensible low-order model for wall turbulence dynamics,” *Phys. Fluids* **26**,  
848 085111 (2014).
- 849 <sup>57</sup> R. A. Antonia and R. E. Luxton, “The response of a turbulent boundary layer to a step change  
850 in surface roughness. Part 2. Rough-to-smooth,” *J. Fluid Mech.* **53**, 737–757 (1972).

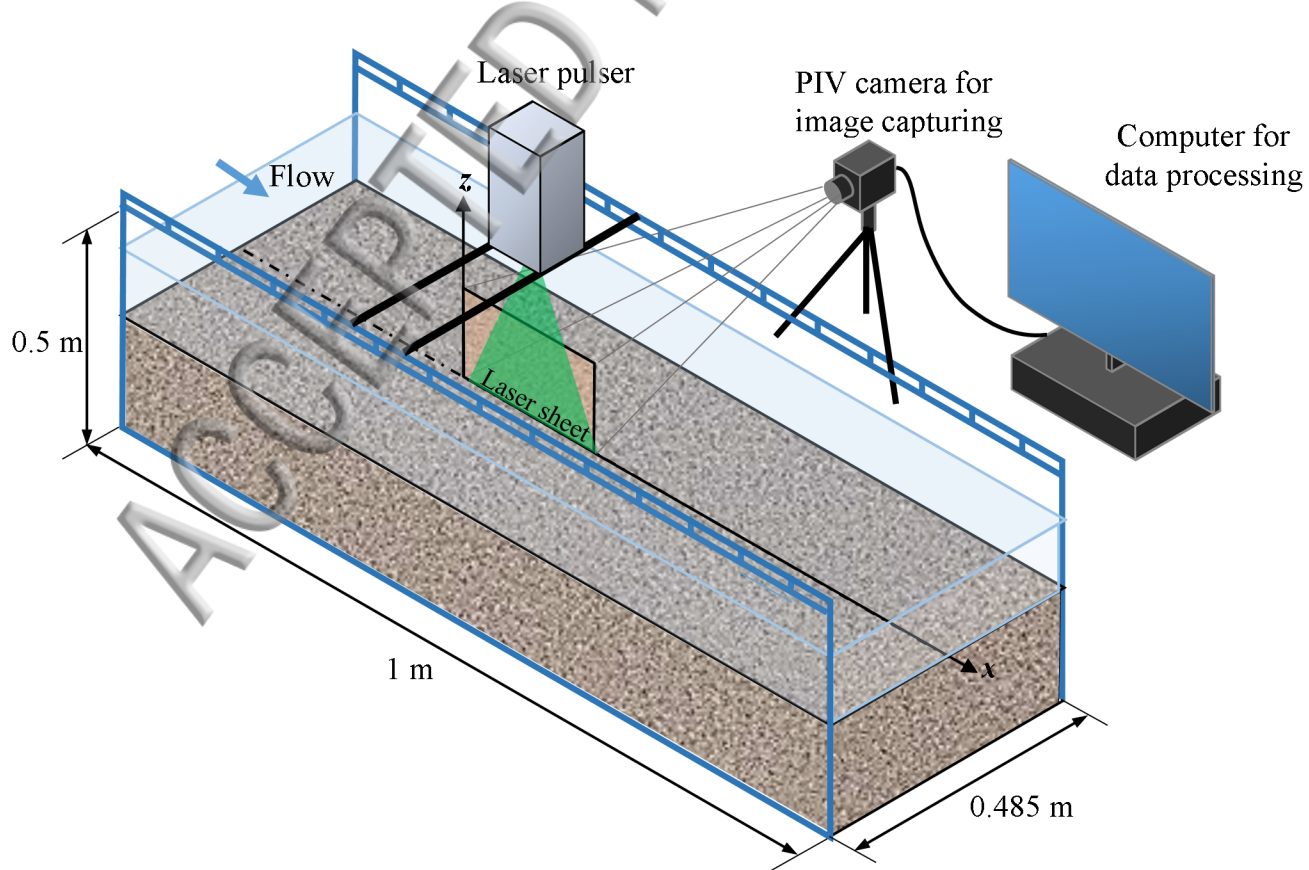
- 851 <sup>58</sup> M. R. Raupach, R. A. Antonia, and S. Rajagopalan, “Rough-wall turbulent boundary layers,”  
852 *Appl. Fluid Rev.* **44**, 1–25 (1991).
- 853 <sup>59</sup> F. Russo and N. T. Basse, “Scaling of turbulence intensity for low-speed flow in smooth pipes,”  
854 *Flow Measure. Instrumt.* **52**, 101–114 (2016).
- 855 <sup>60</sup> N. T. Basse, “Turbulence intensity and the friction factor for smooth- and rough-wall pipe flow,”  
856 *Fluids*, **2**, 1–13 (2017).
- 857 <sup>61</sup> S. Dey and R. V. Raikar, “Characteristics of loose rough boundary streams at near-threshold,”  
858 *J. Hydraul. Eng.* **133**, 288–304 (2007).
- 859 <sup>62</sup> S. Dey and T. K. Nath, “Turbulence characteristics in flows subjected to boundary injection and  
860 suction,” *J. Eng. Mech.* **136**, 877–888 (2010).
- 861 <sup>63</sup> V. Deshpande and B. Kumar, “Turbulent flow structures in alluvial channels with curved cross-  
862 sections under conditions of downward seepage,” *Earth Surf. Processes Landforms* **41**, 1073–  
863 1087 (2016).
- 864 <sup>64</sup> S. Sarkar, A. N. Papanicolaou, and S. Dey, “Turbulence in a gravel-bed stream with an array of  
865 large gravel obstacles,” *J. Hydraul. Eng.* **142**, 04016052 (2016).
- 866 <sup>65</sup> M. A. Reidenbach, M. Limm, M. Hondzo, and M. T. Stacey, “Effects of bed roughness on  
867 boundary layer mixing and mass flux across the sediment-water interface,” *Water Resour.*  
868 *Res.* **46**, W07530 (2010).
- 869 <sup>66</sup> H. Fang, X. Han, G. He, and S. Dey, “Influence of permeable beds on hydraulically macro-rough  
870 flow,” *J. Fluid Mech.* **847**, 552–590 (2018).
- 871 <sup>67</sup> J. Finnigan, “Turbulence in Plant Canopies,” *Annu. Rev. Fluid Mech.* **32**, 519–571 (2000).
- 872 <sup>68</sup> X. Han, G. He, and H. Fang, “Double-averaging analysis of turbulent kinetic energy fluxes and  
873 budget based on large-eddy simulation,” *J. Hydrodyn.* **29**, 567–574 (2017).
- 874 <sup>69</sup> A. M. Fincham, T. Maxworthy, and G. R. Spedding, “Energy dissipation and vortex structure in  
875 freely decaying, stratified grid turbulence,” *Dyn. Atmos. Oceans* **23**, 155–169 (1996).
- 876 <sup>70</sup> C. Manes, D. Pokrajac, I. McEwan, and V. Nikora, “Turbulence structure of open channel flows  
877 over permeable and impermeable beds: A comparative study,” *Phys. Fluids* **21**, 125109  
878 (2009).
- 879 <sup>71</sup> S. Dey, R. Das, R. Gaudio, and S. K. Bose, “Turbulence in mobile-bed streams,” *Acta*  
*Geophysica* **60**, 1547–1588 (2012).

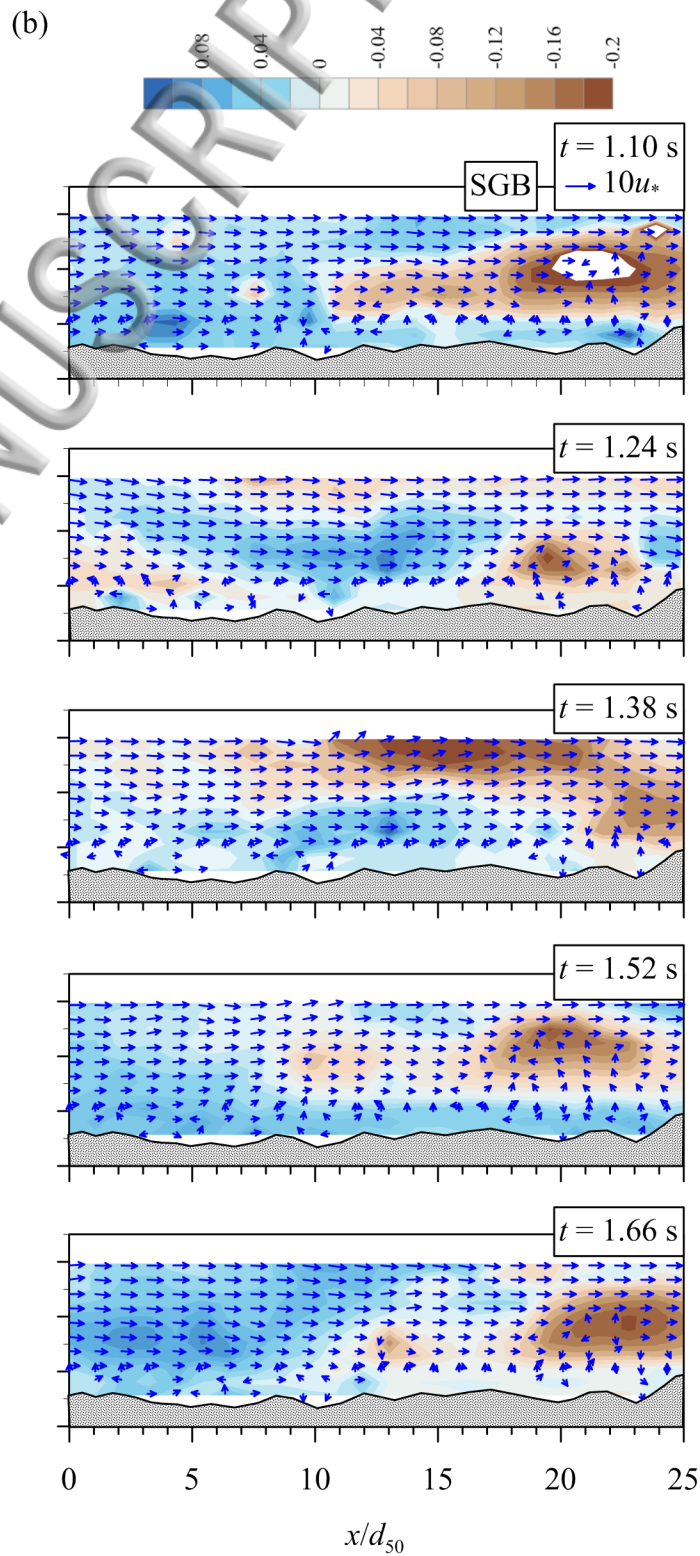
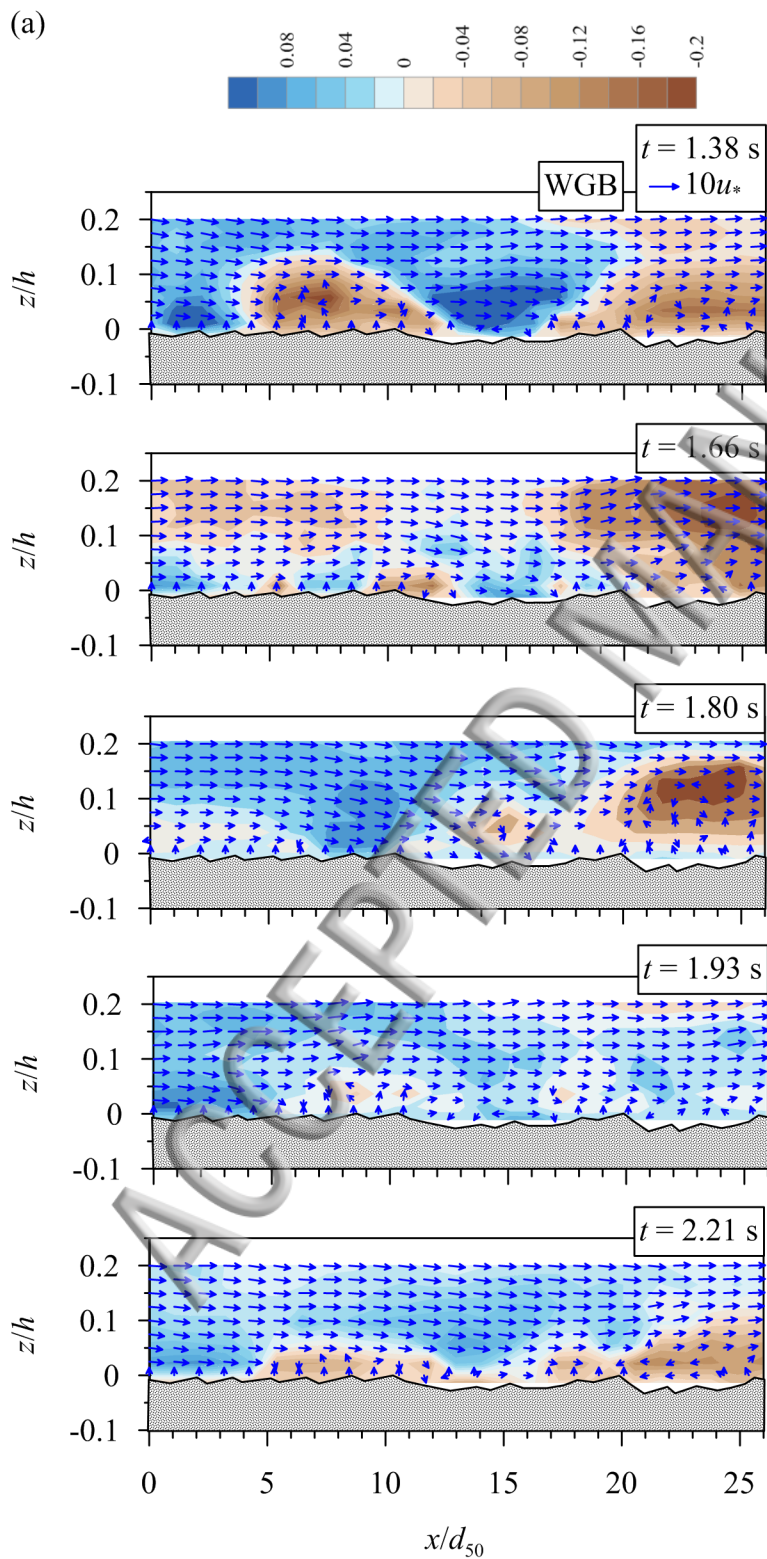
(a)

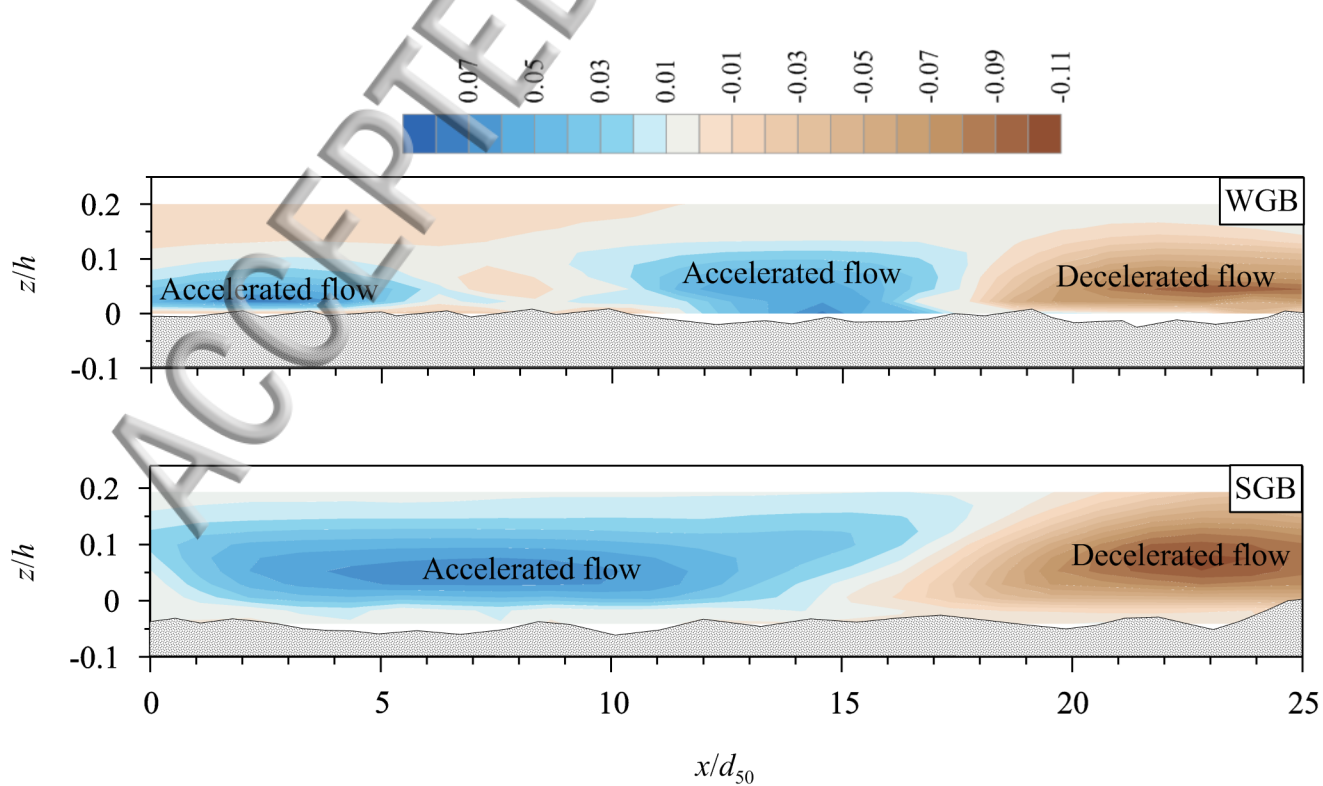


(b)

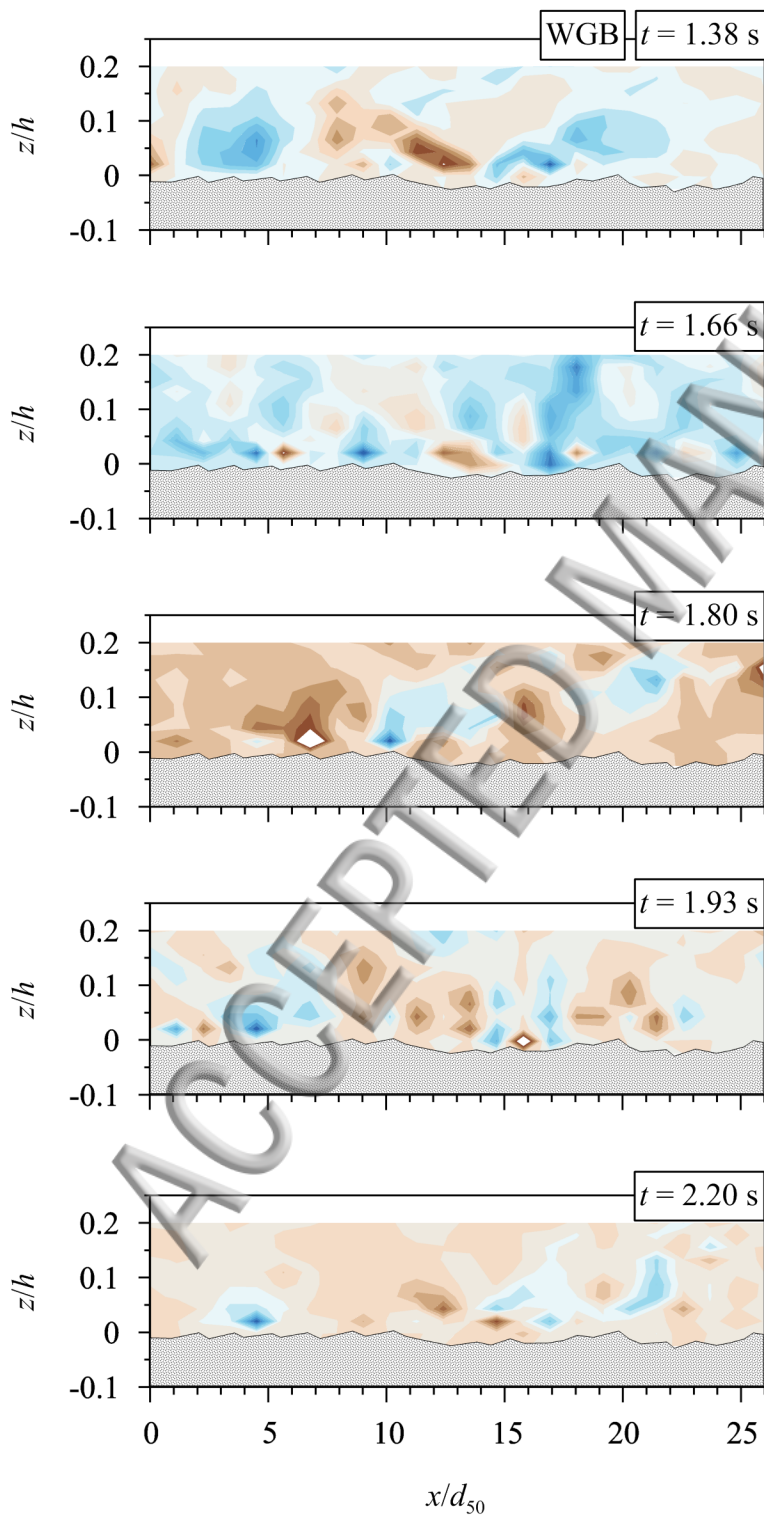
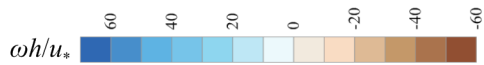








(a)



(b)

